Identifying a Source Assemblage for Buckland Volcanic Province

By

Joshua Shea

A thesis submitted to Macquarie University

for the degree of Master of Research

Department of Earth and Planetary Sciences

15th October 2018

Except where acknowledged in the customary manner, the material presented in this thesis is, to the best of my knowledge, original and has not been submitted in whole or part for a degree at any university.

_____

Joshua Shea

Acknowledgements

I acknowledge the traditional custodians of the Macquarie University land, the Wattamattagal clan of the Darug nation, whose cultures and customs have nurtured, and continue to nurture, the University land, since the Dreamtime. I pay my respects to Elders past, present and future. I am grateful to have been educated on this land, especially to a level capable of writing this thesis.

Steve Foley, thank you for taking me on as a student. You have taught me so much, your work and the way you approach it is huge source of inspiration. I consider myself very lucky to have been supervised by you. Dorrit Jacob, thank you for all of the opportunities you have provided me, you have been an enormous role model for me throughout this degree. Nathan Daczko, you taught me so much, particularly during year one of this degree, thank you for the opportunity to work with you. Kim Jessop, thank you for kindly allowing Steve and I to cut up, crush, and probe your samples. This project would not have been possible without the help of technical staff at MQ GeoAnalytical, particularly Tim Murphy, Peter Wieland, and Yi-Jen Lai.

I would finally like to thank my family. I know you have no idea what I have spent the past ten months doing, but thank you for the blind confidence in letting me follow what I am passionate about. Mum and Dad, you have provided me with so many opportunities throughout life, and I will never be able to repay you. I hope this acknowledgement helps. Christin, thanks for being a supportive sibling throughout this degree.

I have had many friends who have helped me throughout this thesis, whether it has been tolerating my rants about rocks, or letting me know all the work will all be worth it in the end. In no particular order, thank you Kyle, Dean, Bonnie, Chloe, Joey, Maddy, Anthony and Sinan and many more.

Lastly, to the people who I was lucky enough to completed this Masters of Research with. Alice, Ben, Steph, Chris, Tom, and Pete. We did it.

Abstract

Buckland volcanic province lies on lithosphere transitioning from thick > 160 km in the west to < 110 km thick to the east. Similar intraplate volcanic provinces to the north and south show signs of a metasomatised lithospheric mantle source assemblage that produced non-four phase peridotite phases such as amphibole and apatite. This study investigates the role of metasomatism on the lithospheric mantle source assemblage for Buckland volcanic province. Here both whole rock and olivine minor and trace element chemistry is used to better indicate the mineralogy and metasomatic agent of the source assemblage. High whole rock Zr/Hf (range = 50 – 58) and low Ti/Eu (range = 3071 – 8059) trend towards values for natural carbonatite melts. These carbonatite-like values are interpreted as being adopted by the subsequent silicate melts generated in regions affected by carbonatite metasomatism. Three groups of olivines are characterised, peridotitic xenocrysts, alkali basalt olivines, and basanite olivines. Olivine xenocrysts Sc/Zr and Al/Mn are characteristic of a spinel lherzolite peridotite assemblage. Olivine phenocrysts $Fo_{73–87.5}$ from both the alkali basalts, and basanites have concentrations of Li, Zn, Ti and Mn/Fe indicating the presence of mica in the source assemblage. While elevated Ni is characteristic of high modal pyroxene, and Ni/Mg and Mn/Fe suggest both mica and pyroxene in the source assemblage are mixed with peridotite wall rock components to produce the Buckland primary melt. It is suggested here that the source assemblage from the Buckland Volcanic Province is spinel lherzolite veined by a varying amounts of pyroxene-glimmerite ± apatite, for both the alkali basalts and basanites. This suggests mica has a larger role in intraplate basalt source assemblages, and agrees with literature that metasomatism plays a large role in the generation of intraplate basalts in eastern Australia.

Contents

List of Figures

List of Tables

Chapter 1

Introduction and previous work

> *"A primary melt is the melt composition in equilibrium with its source at the time of extraction."*
>
> – Foley and Pintér (2018)

Primary melts are expressed on Earth's surface as solidified magma and their chemistry holds clues that are useful to decipher a mantle source assemblage not expressed on the surface (Kelemen et al., 1998; Herzberg, 2011). To identify a source assemblage of a melt, the composition of its primary melt needs to be well understood since they are in equilibrium at the time of extraction (Foley and Pintér, 2018). Olivine is the first silicate phase to crystallise in a mantle-derived melt, so its minor and trace element concentrations in primitive (high mg-number (100Mg/(Mg + Fe))) olivines capture the earliest representation of a primary melt composition with little to no fractionation effects (Sobolev et al., 2005). In recent years, minor and trace elements in olivine have formed key components for the argument that mantle source assemblages have non-peridotite components (Foley et al., 2013). This argues peridotite is not the only relevant rock type melting in the upper and subcontinental lithospheric mantle (Herzberg, 2011; Sobolev et al., 2005, 2007; Straub et al., 2008).

Eastern Australia represents one of the world's most extensive intraplate continental volcanic regions stretching 4,400 km from northern Queensland to southern Tasmania (Figure 1.1; Johnson and Wellman, 1989; O'Reilly and Griffin, 1987). Fifty different intraplate volcanic provinces have been identified in eastern Australia, which have been dated between 65 Ma and 5000 BP, consisting mainly of mafic rocks, from highly under-saturated leucitites to *qz*-tholeiites (Wellman and McDougall, 1974; Johnson and Wellman, 1989), to alkali basalt and basanites with MgO > 7.5 wt. % and high enough to be considered primary mantle melts (Skae, 1998). Hitherto, no studies have targeted high mg-number olivines from eastern Australia to identify their mantle source assemblages. However, previous work on bulk rock compositions has shown metasomatic events underneath eastern Australia (Frey and Green, 1974; Frey et al., 1978), and the presence of apatite and phlogopite in some mantle source assemblages (O'Reilly et al., 1988; O'Reilly and Griffin, 2000; Zhang and O'Reilly, 1997). The use of olivine minor and trace elements may add accuracy to understanding a primary melt composition, and

help identify non-peridotite components, such as pyroxenite or glimmerite, that may have contribute to a primary melt.

This thesis uses olivine and whole rock chemistry from the Buckland Volcanic Province (Buckland), Queensland, Australia, to identify its mantle source assemblage (Figure 1.1). Buckland is the most southern intraplate volcanic province in central Queensland, and lies on thick continental crust ~125 km in a zone transitioning from thick cratonic crust > 160 km to thinner crust < 110 km towards the east coast of Australia (Davies et al., 2015). Thick continental crust absorbs incipient melts which metasomatises the sub-lithospheric mantle creating non-peridotite domains that may contribute to the formation of subsequent primary melts (Foley and Pintér, 2018; Yaxley and Green, 1998). Buckland is therefore a prime intraplate volcanic province to investigate if non-peridotite components contributed to its source assemblage. The combination of bulk rock chemistry with olivine chemistry will hopefully add new approaches to the emerging field using olivine minor and trace elements to better identify mantle source assemblages.

The remainder of this chapter is separated into two broad parts that form a holistic foundation for the overall aim of this thesis. The first part introduces the olivine structure, its chemistry, and controls on minor and trace element partition into olivine, which is critical to understand its usefulness as a source assemblage indicator. The second part is an overview of intraplate volcanism in eastern Australia, previous work on source assemblage identification for eastern Australian intraplate volcanic provinces and previous work on Buckland.

1.1 Introduction to the olivine structure and its chemistry

Olivine is an orthosilicate mineral with a solid solution between the two end members forsterite (Mg_2Si0_4; Fo_{100}), and fayalite (Fe_2Si0_4; Fa_{100} or Fo_0; Deer et al., 1997). The olivine crystal structure consists of independent $Si0_4$ tetrahedra (T sites) linked by divalent atoms in a six-fold coordination site (M site); described as a M_2TX_4 (Birle et al., 1968). There are two, non-equivalent six-fold coordinate positions in an olivine unit cell, which are designated as M_1 and M_2 (Burns, 1970; Deer et al., 1997). Both M sites are distorted, leading to the M_1 site being regarded as a tetragonally distorted octahedron elongated along the O_3-O_3-axis, and the M_2 site being regarded as a trigonally distorted octahedron, compressed along the a-axis (see Figure 1.2; Burns, 1970). Different distortion effects on each M site result in the M_1 site being slightly smaller than the M_2 site (M_1 = 73 pm; M_2 = 76.7 pm; see Figure 1.2; Birle et al., 1968).

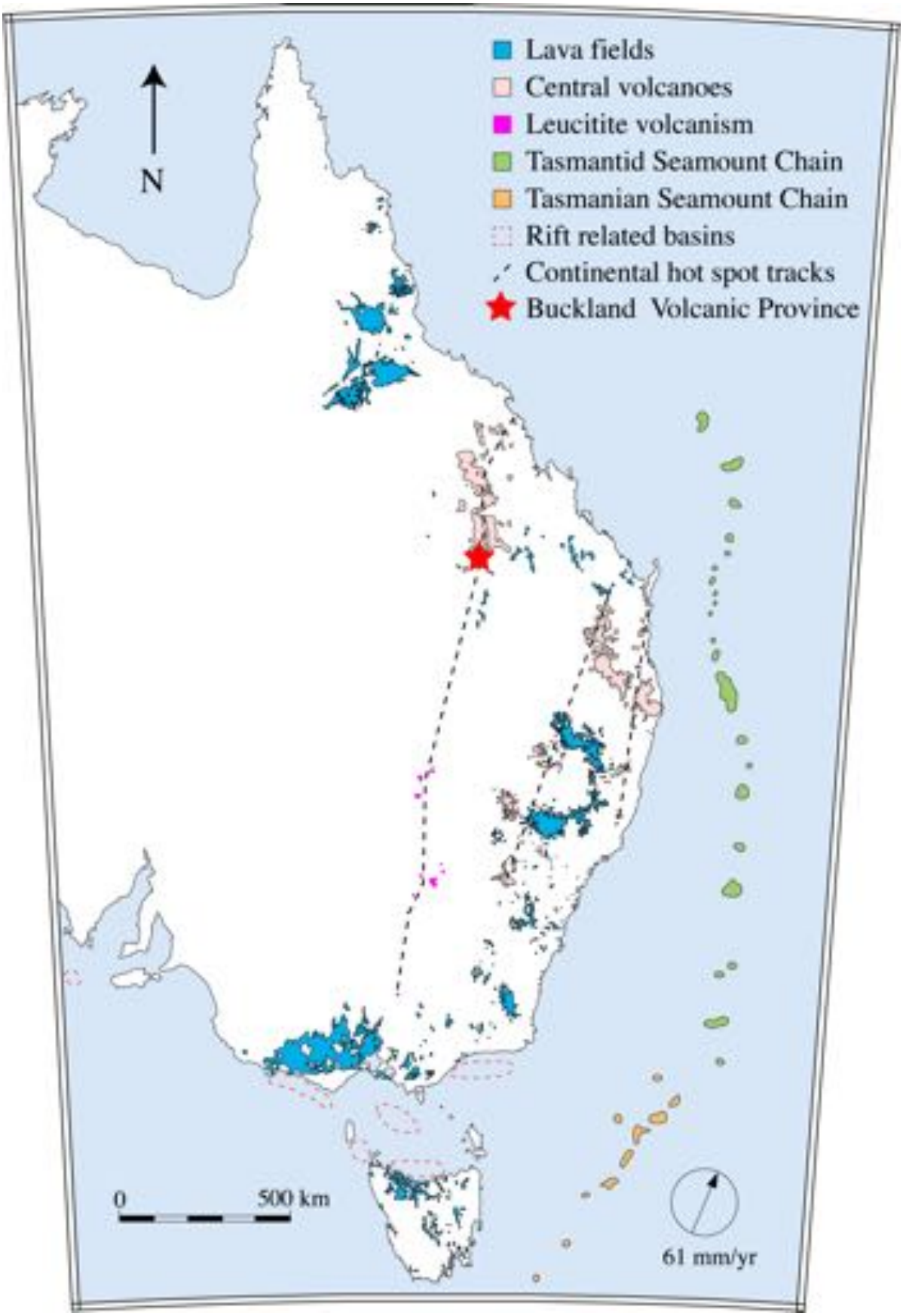

Figure 1.1: The distribution and classification of Cenozoic volcanic provinces, seamounts, proposed hotspot tracks, and rift-related basins in eastern Australia. Adapted from Davies et al. (2015); Johnson and Wellman (1989); Meeuws et al. (2016); O'Reilly and Griffin (1987).

The only significant major element variation in olivine lies between the two end-members of its solid solution, forsterite, and fayalite, which substitute into olivines M sites (Birle et al., 1968; Deer et al., 1997; Zanetti et al., 2004). In a mantle-derived melt, forsterite is the first silicate mineral to crystallise, as olivine crystallises the melt becomes progressively depleted in Mg, resulting in subsequent olivine being more fayalite-rich (Birle et al., 1968; Green and Ringwood, 1963). Whereas olivine xenocrysts from mantle peridotites generally have $Fo_{\geq 90}$ (Bussweiler et al., 2017). The forsterite molar percentage of olivine is expressed as either mg-number ($Mg^{\#}$) or Fo (Fo mol. %; Fo_{XX}). The Fo mol. % is directly correlated with the Fe-Mg concentrations of the olivines parental melt, with a $D^{ol/liq}_{Fe^{2+}-Mg}$ = 0.30 for most basaltic melts (Roeder and Emslie, 1970). Palme and O'Neill (2014) identified primitive mantle values for olivine Fo mol. % from spinel lherzolite using a half Gaussian distribution of samples from the Geochemistry of Rocks of the Oceans and Continents (GEOROC) database (http://georoc.mpch-mainz.gwdg.de/georoc/), finding the primitive mantle value for olivine Fo mol. % to be $Fo_{89.0\pm0.001}$ for the primitive upper mantle. They also stated melt infiltration or metasomatism lowers, and melt extraction increasing this value. The ambiguity of defining between phenocrysts and xenocrysts of olivines with $Fo_{>89.0}$ generally invokes minor and trace element classifications, with the most widely used being those from either Foley et al. (2013), or Bussweiler et al. (2017) using Ni, Mn, Ca, Al, Ti, Cr concentrations. To identify mantle source assemblages olivine with the highest possible Fo mol. % down to either Fo_{86} (Sobolev et al., 2005, 2007), or Fo_{70} (Herzberg, 2011; Herzberg et al., 2016), are generally targeted. This represents olivine compositions which were the first phase crystallise and olivines which underwent the initial effects of fractionation Fo< 88 (Bussweiler et al., 2017; De Hoog et al., 2010).

Minor and trace element concentrations vary widely in the olivine structure. Most substitutions take place on the M sites with divalent ions of similar sizes, however large ions and ions with different oxidation states may form coupled substitutions, such as (Si^{4+}, Mg^{2+}) ↔ (Al^{3+}, Cr^{3+}), (Si^{4+}, Mg^{2+}) ↔ (Al^{3+}, Al^{3+}), and 2(Mg^{2+}, Mg^{2+}) ↔ 2(Na^{+}, Al^{3+}) (De Hoog et al., 2010; Matzen et al., 2017; Taura et al., 1998). Further coupled substitutions have been suggested for trivalent ions, which include M site vacancies, including Sc^{3+} and the rare-earth-elements (REE), e.g. ($2Sc^{3+}$ + M site vacancy) ↔ 3(Mg^{2+} or Fe^{2+}) (Nielsen et al., 1992). The substitution of Ti^{4+} in olivine has received special attention due to its correlation with water content in olivine under experimental mantle conditions (Berry et al., 2005, 2007a). Under anhydrous conditions Ti can substitute into either the M site, or T site (Figure 1.2), however under hydrous conditions Ti^{4+} predominately substitutes Si at the T site forming a Ti-clinohumite-like ($Mg_2TiO_2(OH)_2$) point defect in olivine, which Berry et al. (2007b)

observed in upper mantle spinel peridotites.

1.2 Analytical methods for olivine minor and trace element measurements

Olivine minor and trace elements have become a topic of discussion due to the development of techniques which allow low concentration *in situ* analysis. Sobolev et al. (2005, 2007) used electron-probe micro analysis with high charges, and has led to the common use of a high-precision electron-probe micro analysis (HPEPMA) protocol on olivines (Batanova et al., 2015). This development has produced large datasets of Al, Ca, Cr, Mn, Co, and Ni concentrations in olivine, mainly from ocean island settings. Later studies optimised laser-ablation inductively-couple-plasma mass-spectrometry (LA-ICP-MS) to detect more incompatible suites of olivine trace elements (Foley et al., 2011), with more recent protocols detecting ultra-trace concentrations of rare-earth-elements (REE) in olivine (Stead et al., 2017). Lower detection limits for improved protocols allow for more trace elements and even ultra-trace element information becoming detectable, quickly giving rise large datasets on early magmatic histories and mantle processes. Batanova et al. (2015) discussed the differences between

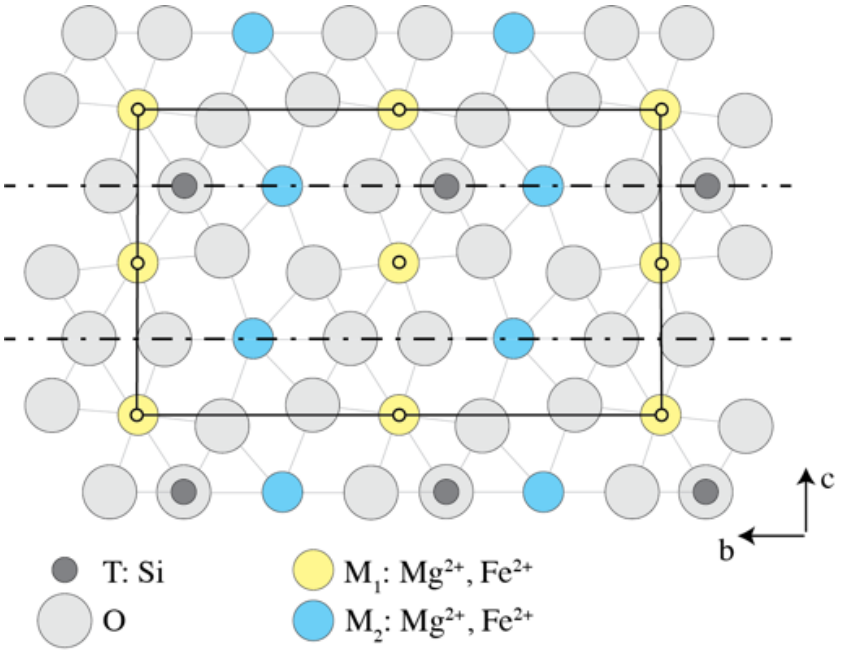

Figure 1.2: A schematic of an ideal olivine crystal structure viewed along the a axis. This figure emphasises the lattice distortions of both the M_1 and M_2 sites, showing the M_2 cation further away from its bonding ligands than the M_1 site. Adapted from Biedermann et al. (2014)

HPEMPA and LA-ICP-MS. HPEPMA has smaller spatial resolution, down to 2 μm, compared to LA-ICP-MS with spatial resolution ranging from 20 μm (Veter et al., 2017) - 300 μm (De Hoog et al., 2010) this proves advantageous for small or highly zoned olivines, and may overcome the possible effects of diffusion. However HPEPMA has much higher detection limits, cannot detect lighter elements, some of which have geological importance, such as Li, and cannot simultaneously measure as many elements as LA-ICP-MS protocols (Foley et al., 2011). Recent studies combine both methods, however measurements on the same grain sometimes differ between the two methods. Fritschle et al. (2013) explains this is due to the different spatial resolutions of the two methods, HPEMPA has a 2 μm beam which penetrates up to 6 μm at 20 kV (Batanova et al., 2015), while a laser ablation crater results in a much larger crater with much more vertical extension which varies depending on the protocol. Some studies such as Neumann et al. (1999), which combine both EPMA and LA-ICP-MS data, have large variations between the two methods, with the LA-ICP-MS data being unrealistically high, especially compared to EPMA data. Differences could be due to a number of variables, and with such a rapidly progressing field care needs to be taken when collecting data to avoid possible contamination and when reading or collecting literature data.

1.3 Controls for minor and trace element concentrations in olivine

Minor and trace elements energetically prefer to substitute into the M sites in olivine (Taura et al., 1998). However, few minor and trace elements have a similar ionic radius to the M_1 and M_2 sites and even fewer have the required divalent charge (Figure 1.3 Foley et al., 2013). This restricts the amount of minor elements to Ni^{2+} (with an ionic radius of 69 pm) and Mn^{2+} (67 pm), and divalent trace elements are usually restricted to cations which are either slightly bigger or smaller than the olivine M sites (Shannon, 1976). As mentioned above, the incorporation of a cation with a radically different ionic radius but similar charge (Ca^{2+}; 100 pm), the incorporation of a cation with a similar ionic size but different charge (Zr^{4+}; 72 pm), and the incorporation of a cation with different size and different charge (Y^{3+}; 90 pm), require either lattice strain to fit larger cations (Wood and Blundy, 2003), or coupled substitutions, which are more energetically unfavourable and thus keep concentrations for these cations low (De Hoog et al., 2010; Foley et al., 2013; Shannon, 1976).

Pressure, temperature, melt composition, and oxidation state affects cation substitutions into olivine (Beattie et al., 1991; Brey and Köhler, 1990; Foley et al., 2013; Matzen et al., 2017; O'Reilly et al., 1997; Taura et al., 1998). Temperature effects have been recognised for Ca, Cr, Ti, Al, Na, V, and REE

to varying degrees (Brey and Köhler, 1990; De Hoog et al., 2010; O'Reilly et al., 1997). Temperature effects have also been seen in Sc and Cr in spinel peridotites, while pressure effects have been seen for mono-, tri-, and tetravalent cations Li, Na, Cr, V, Sc, Al, Y, Zr and Ti (De Hoog et al., 2010; Taura et al., 1998). Both pressure and temperature effects have also been found for Ca (O'Reilly et al., 1997; Taura et al., 1998), and Al (Taura et al., 1998), which casts some doubt on the Ca in olivine geobarometer (Brey and Köhler, 1990), and emphasises for the right application for the Al in olivine geothermometer which is only applicable to garnet lherzolites (De Hoog et al., 2010; Bussweiler et al., 2017). Vanadium is used a monitor of oxidation state, since it has multiple oxidation states that can partition into olivine, since it becomes more compatible in reduced conditions where V^{3+} is available (Foley et al., 2013; Papike et al., 2005; Laubier et al., 2014). V has widely been compared to Sc (Papike et al., 2005), and recently to Yb (Laubier et al., 2014) in olivine as an oxidation indicator. Both Sc and Yb, have minor to no effect on partitioning in different oxidation states (Laubier et al., 2014; Papike et al., 2005), which makes V/Sc and V/Yb useful to describe if a primary melt was oxidised or reduced. Composition effects have been found most for divalent transitional metals, Ni, Mn, Co, Zn, Cu, which is thought to be due to crystal field effects that emphasise compositional partitioning more than pressure and temperature (Burns, 1970). However, elements such as Li, Ti, P, and Sr have also had their partitioning behaviour related to melt composition, further arguing compositional effects outweigh pressure and temperature effects on partition depending on the source assemblage (Batanova et al., 2015; Prelević et al., 2013; Sobolev et al., 2005, 2007; Herzberg, 2011). Recently discussion on Ni partitioning into olivine has revealed a slight temperature dependency at low pressures which may lead to variation of olivine Ni concentrations which crystallise underneath thin lithospheric lids (Matzen et al., 2013, 2017). As more elements become detectable from lower detection limits from LA-ICP-MS analysis (De Hoog et al., 2010; Foley et al., 2011), arguments for compositional effects are becoming built on arguments using multiple elements, for example Veter et al. (2017) used multiple minor and trace element indicators in olivine for a phlogopite-rich source assemblage for ultramafic lamprophyres in Labrabor.

Different incorporation mechanisms for minor and trace elements in olivine are only useful if zoning is preserved (De Hoog et al., 2010; Foley et al., 2013). Diffusion in olivine widely varies depending on the element, from relatively fast (e.g. Li) to extemeley slow (e.g. P and Ti) (De Hoog et al., 2010; Foley et al., 2013; Prelević et al., 2013; Mallmann et al., 2009; Cherniak and Liang, 2014). Generally slow diffusing elements are regarded as good source assemblage indicators since the best preserve minor and trace element concentrations from inital olivine crystallisation Batanova

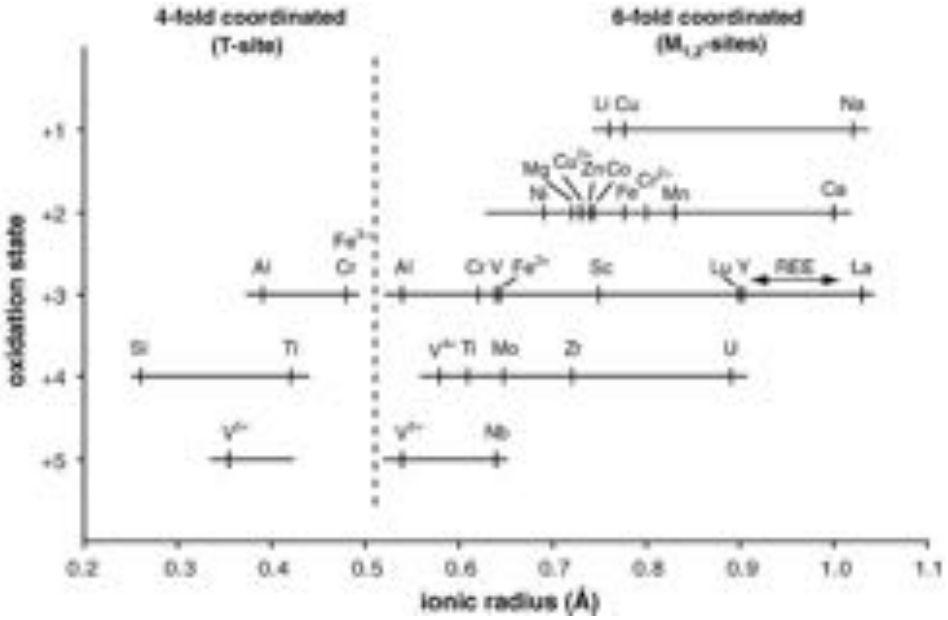

Figure 1.3: A schematic of the oxidation state and ionic radii for cations that substitute into the olivine structure. Reproduced from De Hoog et al. (2010)

et al. (2015); De Hoog et al. (2010); Foley et al. (2013). However, if a mantle source assemblage is inferred to have formed shortly before eruption, and the olivine phenocrysts are measured relatively quickly after formation, fast diffusing elements, such as Li may be used (Foley et al., 2013; Jaques and Foley, 2018). However, further research is needed into poorly studied elements such as P, which may provide further insight into the preservation of zoning in olivine and which elements preserve the most appropriate evidence to indicate a mantle source assemblage.

1.4 Using olivine minor and trace elements as source assemblage indicators

1.4.1 Peridotite assemblages

Minor and trace elements in olivine xenocrysts from four phase upper mantle peridotites can distinguish between each peridotite facies (De Hoog et al., 2010). Olivines crystallised in primary melts derived from an upper mantle four phase peridotite have been widely studied and modelled using fractional crystallisation and batch melting models based on primitive upper mantle compositions from McDonough and Sun (1995) (Straub et al., 2008; Herzberg, 2011; Herzberg et al., 2016). De Hoog et al. (2010) characterised olivine xenocrysts from different peridotite facies and effectively

discriminated between each facies by comparing concentrations of Zr and Sc, and Mn and Al. Garnet peridotite xenocrysts generally contains low concentrations of Sc and Mn, with high Zr and Al; garent-spinel peridotite xenocrysts contain low Sc, Zr, Al, and Mn; and, spinel peridotite xenocrysts have high Sc, Mn, and Al, with low Zr. Herzberg (2011), and Herzberg et al. (2016) modelled olivine minor elements which crystallised in a primary melt derived from a peridotite source assemblage based on primitive upper mantle values from McDonough and Sun (1995), while Straub et al. (2008) and Herzberg et al. (2016) additionally accounting for peridotite source depletion and magma mixing events. These models are mainly used to show olivine minor element concentrations deviated from a primary melt derived from a peridotite source assemblage, and to invoke input from a metasomatised domain into the primary melt.

Minor and trace element differences between olivine xenocrysts and phenocrysts are useful to distinguish *in situ* olivine phenocrysts from mantle xenocrysts (Bussweiler et al., 2017; De Hoog et al., 2010). Bussweiler et al. (2017) used a major and minor element scheme for identifying mantle peridotite xenocrysts; $Fo_{\leq 90}$, NiO $\leq$ 0.3 wt. % ($\leq$ 2350 ppm), MnO $\leq$ 0.15 wt. % ($\leq$ 1160 ppm), and CaO $\leq$ 0.1 wt. % ($\sim$ 715 ppm). While Foley et al. (2013) showed mantle olivine xenocrysts from peridotite assemblages typically have < 70 ppm Ti, Ni ranging 2200 – 3400 ppm, and $\sim$ 80% contain < 130 ppm of Al. This is a useful tool when using olivine phenocrysts to identify a mantle source assemblage since a xenocrysts identified as a phenocrysts may result in a poor identification of a mantle source assemblage. These schemes are good for identifying peridotite xenocrysts, however they may be problematic when identifying olivine xenocrysts from depleted or enriched peridotites, and non-peridotite domains (Palme and O'Neill, 2014).

1.4.2 Recycled oceanic crust components in source assemblages

Peridotite material is usually contributes to a primary melt, and can be diluted by another non-peridotite component, than may have formed from metasomatism driven by the recycling of oceanic crust and other down going material (Foley and Pintér, 2018). The influence of eclogite/metasomatised pyroxenites are the most well studied non-peridotite source assemblage using olivine minor and trace elements. Sobolev et al. (2005) first used HPEMPA to measure Ni and Fe/Mn concentrations to argue for an olivine-free metasomatised pyroxenite assemblage for Hawaiian shield basalts. This was predicated on the idea that the tholeiites material was too SiO_2-rich (average = 48.4 wt. %) and Ni-rich (average = 827 ppm), and contain olivines with high Ni and Fe/Mn, and this could not occur by only melting peridotite (Sobolev et al., 2005). High-Ni and Fe/Mn olivines crystallise in a melt where

olivine is either absent or in low modal abundance in the source assemblage so elements which olivine would have otherwise held back in the residue now contribute to the melt (Sobolev et al., 2005, 2007). This partial melt meatsomatically enriched in elements compatible in olivine held identify low-olivine source assemblages. Sobolev et al. (2005) and later Sobolev et al. (2007) used this concept to argue metasomatic pyroxenites contribute to primary melts for many ocean island basalt settings worldwide and have been derived from recycled crust entrained in mantle plumes; this idea has been dubbed the “Sobolev model" throughout the literature.

The Sobolev model describes an adiabatically rising mantle parcel consisting of heterogeneous peridotite and eclogite domains. The more fertile eclogite domain is the first to extensively melt, producing a SiO_2 and Ni-rich partial melt, which reacts with the surrounding peridotite, precipitating pyroxene and producing zones of olivine-poor and olivine-free metasomatic pyroxenites. Continued adiabatic up welling drives partial melting of the metasomatic pyroxenite veins preferentially to peridotite wall-rock material. The derived primary melts consist of both pyroxenite, and depending on the degree of melting, peridotite wall rock material. Later studies have amended this model for different geodynamic settings. For example, Straub et al. (2008) modified this for the production of basalts and andesites in arc settings, from the mixing of pyroxenite and depleted peridotite.

Herzberg (2011), Herzberg et al. (2013, 2014, 2016), and (Straub et al., 2008) reinforce the Sobolev models use of olivine trace elements for identifying pyroxenite material by modelling trace element concentrations in olivine at different mg-numbers using partition coefficients from peridotite and pyroxenite datasets. Herzberg (2011) first pioneered modelling Ni, Fe/Mn, and Ca in olivine to show the high-Ni Hawaiian olivines from Sobolev et al. (2005) deviate from a primitive upper mantle assemblage; agreeing there is a good case for a heterogeneous metasomatised pyroxenite and peridotite wall-rock source assemblage for Hawaiian shield basalts. Straub et al. (2008) showed that in an arc setting andesites in the Trans Mexican Volcanic Belt are the result of a heterogeneous pyroxenite/peridotite assemblage in the mantle wedge, by calculating the depletion of the peridotite component and the mixing between both peridotite and pyroxenite components. However, the subtle changes in D_{Ni} and and the large errors involved in minor and trace element modelling can result in multiple plausible scenarios. For example, Herzberg et al. (2016) showed Ni in olivines from the West Greenland and Icelandic plumes could be interpreted by Ni enrichment in the source plume from a core-mantle boundary interaction (see Herzberg et al., 2014), or could be interpreted as an elevation in $D_{Ni}^{ol/liq}$ from lithospheric under-plating shown by Matzen et al. (2013).

1.4.3 Other non-peridotite components in source assemblages

Overtime, the subcontinental lithospheric mantle absorbs infiltrating incipient melts that are unable to reach the surface which drives mantle metasomatism (Foley and Pintér, 2018). The fluxing of these melts, and the solidification of incipient melts form non-peridotite domains that range from centimetre veins to large metre scale, blocks, conduits, dikes, or sills of non-peridotite assemblages, some of which may have never been observed on the surface (Foley and Pintér, 2018). These non-peridotite components have a lower melting point due to silica and aluminous concentrations, and enrichments in incompatible elements and volatile components which are likely contained in amphibole ± mica ± clinopyroxene ± apatite ± Cr-spinel (Frey et al., 1978; O' Reilly, 1987; Yaxley et al., 1998). Significant H_2O content in the infiltrating melt drives the stability of hydrous phases, primarily phlogopite/biotite and amphibole, and elevated CO_2 may lead to dolomite, and magnesite stability (Foley, 1992; Wyllie et al., 1983). Primary melts derived from these areas in the lithosphere are usually a mixture of non-peridotite and peridotite domains, with the degree and depth of melting controlling the proportion of each component (Foley, 1992).

Elevated Ni has been pioneered as an indicator for recycled oceanic floor basalts, however D_{Ni} increases 5-6 times in highly alkaline melts (see Foley et al., 2011; Förster et al., 2018), which can only be accounted for by melting of an unrealistically depleted (70% depletion) peridotite (Foley et al., 2013; Straub et al., 2008). The most well studied olivines from alkaline melts are from the eastern and western Mediterranean lamproites (Ammannati et al., 2016; Foley et al., 2011), and the Labrodor aillikites, and the Ni, Fe/Mn concentrations in olivine are best explained by phlogopite in the source assemblage (Veter et al., 2017). Elevated Li (>3 ppm) in olivine together with Li and Sr isotopes (Prelević et al., 2013), are best explained by continental crust material recycled in an arc setting from the Mediterranean (Foley et al., 2013). However, the Labrador aillikites occur at the edge of a rifted craton, and their olivine minor and trace element concentrations are best explained by crystallising in a primary melt derived from a source assemblage rich in phlogopite and low modal pyroxene. This non-peridotite domain was attributed previous lamporitic melts solidifying at the base of the cratonic lithosphere during a previous stage of igneous activity (Veter et al., 2017).

Olivine is the first silicate phase to crystallise from a mantle derived melt, however in a Cr saturated melt Cr-spinel may crystallise first (Onuma and Tohara, 1983). Foley et al. (2013) showed Mediterranean lamproites have both low, and high Cr concentrations in high mg-number olivines ($Fo_{>85}$), low Cr concentrations were explained by Cr-spinel crystallisation prior to olivine. Due to the high compatibility of Cr in Cr-spinel ($D_{Cr}^{spinel/liq}$ = 240, Horn et al. (1994) (Table 1.1)), the olivines

which subsequently crystallised were depleted in Cr. Primary melts with high Cr are therefore inferred to have source assemblages with high modal Cr-spinel or other Cr-rich minerals.

Table 1.1: Partition coefficients for first row transition elements mantle minerals. Data complied by Foley et al. (2013), and references therein. Values are for partial mantle melts from peridotite, data is controlled for bulk and melt compositions, oxygen fugacities, temperatures, and pressures. Cr-spinel D_{Mn}/D_{Fe} value may vary up to 0.9 depending on Al_2O_3 and Cr_2O_3 contents, measurements here are based on >40% Cr_2O_3 (Horn et al., 1994; Foley et al., 2013).

Mineral/melt	ol	opx	cpx	grt	Cr-spl	ol/opx
Sc	0.23	0.64	1.40	2.7	0.6	0.36
Ti	0.0016	0.64	0.363	0.43	2	0.15
V	0.09	0.80	1.3	1.7	0.8	0.11
Cr	0.96	5.9	3.8	4.1	240	0.16
Mn	0.89	0.84	1.0	0.65	2.1	1.06
Fe	1.09	0.75	0.80	0.36	4.9	1.45
Co	3.0	1.6	1.4	1.67	5.4	1.88
Ni	10.3	2.83	2.35	4.0	20	3.63
Cu	0.50	0.22	0.42	0.58	0.42	2.27
Zn	1.1	0.67	0.47	1.21	3.3	1.64
Mn/Fe pref.	0.82	1.12	1.25	1.81	0.43	
Mn/Fe (Le Roux et al., 2011)	0.73	1.12	1.56			

Sobolev et al. (2007) used high Ni/Co ($\geq$20) in olivine as an indicator for metasomatised pyroxenites, however (Foley et al., 2013) shows $D_{Ni/Co}^{Cr-spinel/liq}$ = 4 (Horn et al., 1994), so prior Cr-spinel crystallisation would suppress an otherwise elevated Ni/Co in olivine form high modal pyroxene contribution to a primary melt. Fritschle et al. (2013) showed phlogopite has Ni/Co up to 35 and high Cr concentrations that is associated with carbonatite mantle metasomatism, which can also drive high Ni/Co. The migration of H_2O- and/or CO_2-rich fluids and melts have been attributed to the formation of veins containing significant modal pyroxene, phlogopite, amphibole and apatite (Foley, 1992). Olivines that crystallise in a primary melt derived from a non-peridotite assemblage, other than pyroxenite, may interfere source assemblage indicators. For example, Cr-spinel precipitation prior to olivine will interfere minor and trace element indicators in olivine; such as, high-Ni, high-Fe/Mn, and high Ni/Co indicators for low-olivine high-pyroxene pyroxenite assemblages (Sobolev et al., 2005, 2007). This also may be the case for other non-peridotite assemblages which may hold back phases such as phlogopite in the residue.

The identification of non-peridotite minerals and source assemblages can give unprecedented insight into mantle metasomatism and the role of mantle heterogeneity in the production of primary mantle melts. Olivine minor and trace element indicators provide a novel way to investigate possible mantle metasomatism, and lithospheric mantle composition without the need to sample xenoliths, of which, usually succumb to sampling bias (Griffin and O'Reilly, 1986). New analytical advances

continue to improve minor and trace element data from olivine needed to identify key minerals in mantle assemblages.

Na, Ca, Sc, Ti, V, Cr, Mn, Co, Ni, and Zn show promising results that may identify diverse minerals, and may be applied differently depending on a particular different geodynamic settings (Batanova et al., 2015; Cherniak and Liang, 2014; Mallmann et al., 2009). Along with experiments representing likely real-world settings, the identification of partition coefficients for elements that occur in trace and ultra-trace concentrations in olivine may unlock further mineral and mantle metasomatic indicators.

1.5 Introduction to eastern Australian Intraplate volcanism

Intraplate volcanism forms a 4,400 km band of over fifty volcanic provinces along eastern Australia, which erupted onto Proterozic to Mesozoic basement material (see Figure 1.1; Davies et al., 2015; Johnson and Wellman, 1989; Meeuws et al., 2016; O'Reilly and Griffin, 1987). Volcanism began 65 Ma following rifting which opened the Tasman Sea, and became dormant 4,600 BP at Mount Gambier, southern Victoria (Vasconcelos et al., 2008; Johnson and Wellman, 1989). Wellman and McDougall (1974) estimated the total volume of intraplate volcanism in eastern Australia at slightly greater than 20,000 km^3; which is relatively small when compared to estimates from the Deccan Traps (>1,000,000 km^3), and Mouna Loa, Hawaii (~40,000 km^3) (data complied by Johnson and Wellman, 1989; Skae, 1998). Wellman and McDougall (1974) separated eastern Australia's intraplate volcanism into three provincial types: (1) central volcanoes, where predominately basaltic flows were erupted from a well defined vent area, with the presence of some felsic flows, and felsic and mafic intrusions, forming large volcanic complexes. (2) lava fields, extensive and often thin lavas that are exclusively basaltic material and often categorised by the presence of small amount of scoria, lava cones and maars; and (3) leucitite volcanism, small well-spaced potassium rich mafic intrusions commonly containing leucitite, phlogopite, and magnophorite with rare flows of limited extent and small volume.

The understanding of intraplate volcanism in eastern Australia has led to multiple models of emplacement, with no single model able to explain all Cenozoic provinces. (1) The hotspot model, which has been successful in accounting for linear age-progressive tracks for the central volcano provinces (see Figure 1.4; Wellman and McDougall, 1974; McDougall and Duncan, 1980; Sutherland, 1981). (2) Edge-driven convection, which has been proposed to describe isotopic anomalies and large volumes of lava for many large lava fields, such as the newer volcanic province in southern

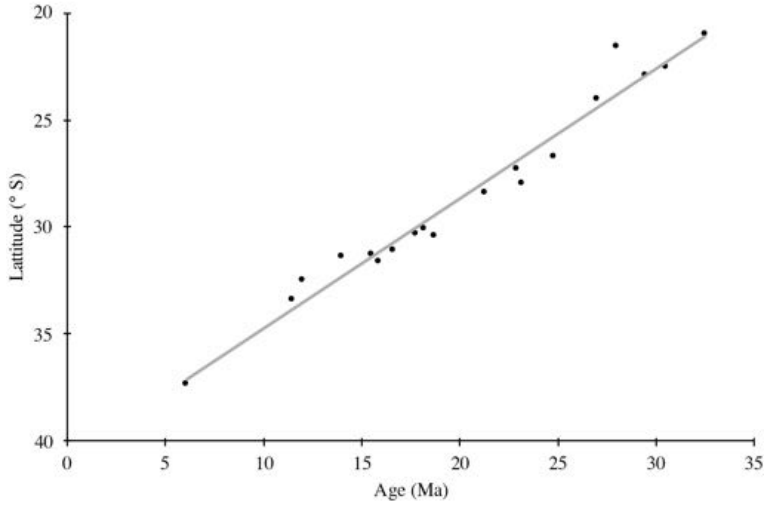

Figure 1.4: Latitude vs. Age plot of the average ages from central volcanoes in eastern Australia. Plotted data from Wellman and McDougall (1974).

Victoria (Davies and Rawlinson, 2014; Demidjuk et al., 2007; Fishwick and Rawlinson, 2012). (3) Slab detachment. The least substantiated model, slab detachment from a prior destructive plate margin occurred $\sim 130 - 90$ Ma (Gurnis et al., 1998) along the northern margin of eastern Australia, and the detachment and sinking of subducted cold oceanic material lead to subsequent up-welling of small local plumes which penetrated weak points in the eastern Australian continental crust forming the lava field volcanism (Finn et al., 2005).

Hotspot volcanism is widely used as a reference frame for high-resolution plate velocity record throughout the Cenozoic, and has been used to explain the production of a large quantity of intraplate igneous rocks in eastern Australia (Cohen et al., 2013). Wellman and McDougall (1974), and a number of later studies, linked the central volcanoes to age progressive tracks, which has been explained by hot-spot volcanism. This led to the Wellman-McDougall model, coined by Sutherland (1981), which describes northward migration of the Australian plate over a fixed mantle hotspot, that is based on latitude-age plots of central volcanoes (see Figure 1.4). This model neatly explains central volcanoes, but ignores lava field, and leucitite volcanism formation. However, recently Davies et al. (2015) linked leucitite volcanism to the age-progressive tracks, and explained their difference in bulk geochemistry and small volume is due to lithospheric thickness, and established large quantities of lava is associated with thinner crust.

Continental lithosphere thickness has long been suspected to influence lava volume and bulk melt composition. Ewart (1989) estimated segregation pressures for different lavas in eastern Australia: 9-14 kbar, *qz*-tholieties; 4-16 kbar *ol*-tholeiites; 16-21 kbar, basanites; 29-31 kbar, nephelinites. Davies

et al. (2015) work was pioneered by recent tomographic work in eastern Australia, which revealed lithospheric thickness is a major variable on composition and volume than previously thought (Davies and Rawlinson, 2014; Davies et al., 2015; Fishwick and Rawlinson, 2012). Davies et al. (2015) linked central volcanoes and lava fields to regions where lithospheric thickness is ≤110 km, where lava compositions range from *qz*-tholeiites to olivine nephlenites (Wellman and McDougall, 1974), while leucitite volcanism is restricted to intermediate lithospheric thickness (≃135 km), with much smaller volumes of lava, with potassium-rich olivine leucitites, and gaps in volcanic activity occurring where the lithosphere exceeds ∼150 km thickness. This development ties each category of volcanic province to a certain lithospheric thickness range.

A single model cannot explain the production of all intraplate volcanism in eastern Australia, and several different attempts have been made to account for the diverse composition of bulk chemistry (Duncan and McDougall, 1989). Frey et al. (1978) was the first to apply fractionation and partial melt models to intraplate basalts to samples from Victoria and Tasmania, and identified that partial melting of a spinel lherzolite could produce the concentrations seen in compatible elements, but strong enrichments in incompatible elements 6 - 9 x chondrite values could only be explained by a prior enrichment. This lead to the idea of two components in the sub-lithospheric mantle in eastern Australia, the first component being a depleted peridotite, and a the second component a liquid enriched in incompatible elements, which enriched the first depleted peridotite component (Frey et al., 1978). This drove the study of mantle xenoliths in eastern Australia, which subsequently identified the role of mantle metasomatism in eastern Australia (Griffin et al., 1987; O'Reilly and Griffin, 1987; O'Reilly and Zhang, 1995; Yaxley et al., 1998; Zhang and O'Reilly, 1997). The enrichment of the sub-continental lithospheric mantle via mantle metasomatism helped explain anomalies in isotope and trace element chemistry, between different provinces along eastern Australia (Figure 1; Davies et al., 2015; O' Reilly, 1987). Rb-Sr, Sm-Nd, and Pb isotope systems, along with whole rock trace element chemistry from Atherton (Whitehead et al., 2007), Dubbo (Zhang and O'Reilly, 1997), and the newer volcanic province (Demidjuk et al., 2007), argue for input from multiple metasomatic sources. Widespread mantle metasomatism in sub-lithospheric mantle beneath eastern Australia has shown the importance of apatite and amphibole, from both silicate, and carbonate fluids, in explaining isotopic and trace element variations; which, may influence the source assemblage of Buckland volcanic province (O'Reilly and Zhang, 1995; O'Reilly and Griffin, 2013).

1.6 Previous work on Buckland Volcanic Province

Buckland volcanic province is a central volcanic province that lies along the Cosgrove hotspot track (Davies et al., 2015), and does not deviate from typical central volcano petrology defined by Wellman and McDougall (1974). Buckland is located ~190 km north-west of Roma, and ~180 km north east of Charleville (Jessop, 2012; Skae, 1998), and is divided into two distinct areas, with massive eruptions from the Buckland shield in the north-east, and distal lava flows thought to have erupted from the shield, which fill Cenozoic topographic depressions (Figure 1.5) (Jessop, 2012). Jones and Verdel (2015) estimated the total volume of Buckland volcanic province to be ~850 km^3, with a lava thickness of 0.3 km.

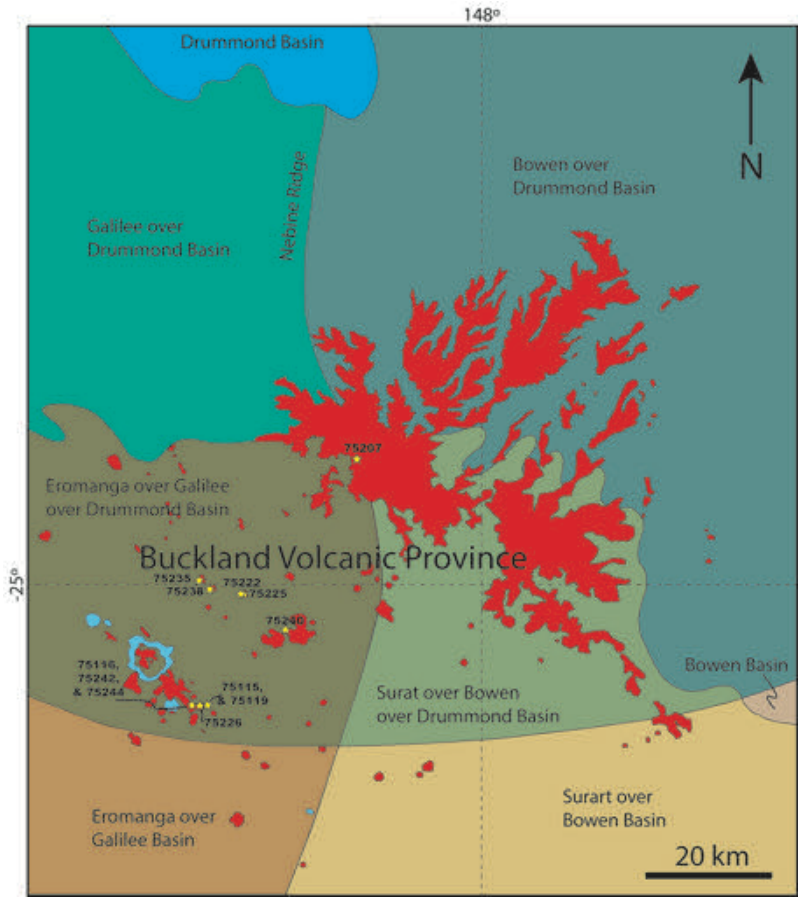

Figure 1.5: A map of Buckland volcanic province showing the tectonic setting, and sample locations (see section 2.1 and 3.1 for more details on samples). Red areas are Tertiary basalts, and light blue areas are gabbro intrusions.

Three major studies have focused solely on Buckland; Skae (1998), a Ph.D. thesis, investigated its petrology, mantle isotope reservoirs, and characterised a possible source assemblage; Waltenburg (2006), an honours thesis, that preformed Ar-Ar dating to distinguish different two seperate eruption events separated by 2 Ma; and Jessop (2012), explored its basalts as a potential source for proximal manganese deposits. A number of other, broader, studies use limited data from Buckland in large

datasets for general characterisations of eastern Australian intraplate volcanism. The remainder of this section will overview our current understanding of Buckland, its general petrology, and potential source assemblages.

Skae (1998) identified two distinct groups of lavas, one group consisting of alkali basalts to olivine tholeiities, and the second group consisting predominately of basanites. The MgO content of the two groups overlap, however there are inconsistencies comparing their isotopic compositions, spider diagram patterns, incompatible trace element ratios, and major element chemistry. The basanites were found to contain higher CaO, and MgO, with lower Al_2O_3 and SiO_2 than alkali basalts, and a single basanite sample suggested a minor magma mixing event occurred. Skae (1998) argued that the most primitive basanite material was sourced from a volatile-bearing lherzolite source assemblage with $X^{H_2O} \leq 0.2$ and H_2O and $CO_2 \geq 0.5$ wt.%, with a HIMU-like arc component, and . Skae (1998) noted that the subduction-accretion history of eastern Australia, since the Palaeozoic, which could have emplaced arc-derived material into the lithospheric mantle, which subsequently produced the Buckland melts during the Oligocene. Lower MgO basanites contained a more enriched Sr-Nd signature which overlaps with lava-field signatures seen in eastern Australia (O'Reilly and Zhang, 1995). The alkali basalt to olivine tholeiite groups are consistent with plume related volcanism, and decompression melting of lherzolite (garnet $\rightarrow$ spinel), under assimilation fractional crystallisation in the crust, with the possibility of some lithospheric and crustal interaction (Skae, 1998). An interesting argument made by Skae (1998) and earlier by Griffin et al. (1987) is that the basanites are similar in isotopic ratios to surrounding lava fields, and that it may be the basanites were erupted during a separate event than the more alkali material to the north-east.

Waltenburg (2006) investigated the idea of separate events for Buckland, describing two distinct volcanic ages in the Buckland volcanic province. The first event erupted between 30.7 Ma ± 0.5 Ma to 29.8 Ma ± 0.4 Ma, followed by a 2 Myr hiatus in which little to no lavas were erupted, and was proceeded by a second eruption event between 27.6 ± 0.6 to 27.3 ± 0.8 Ma (Table 1.2). The first episode of eruptions deposited thin lavas ~100 m thick, with an estimated eruption rate of 108 km^3 Myr^{-1}. The second eruption episode was much larger depositing ~200 m of lava, at a rate of 900 km^3 Myr^{-1}. Waltenburg (2006), similar to Skae (1998), noted two chemically distinct signatures in major element data. The first episode was described as mildly alkaline, higher in Fe_2O_3 and MgO, and lower in Al_2O_3, Na_2O, and TiO_2 than the second volcanic episode. Waltenburg (2006) subdivided the second volcanic episode into two sections, based on two separate chemical signatures. The lower unit of the second episode was described as basanite-type lavas with lower Fe_2O_3 and MgO, and higher

Table 1.2: Ages from Buckland volcanic province. Data Complied by Jessop (2012)

Paper	Location	Method	Age (Ma)
Elliot (1973)	Springwood	K-Ar	26.5 ± 0.5
Sutherland (1985)	Mt Moffat	Zr fission track	27.6 ± 1.0
Sutherland (1987)	Boowinda Creek	K-Ar	27.3 ± 0.4
Sutherland (1989)	The Steeple	K-Ar	25.1 ± 0.4
Waltenburg (2006)	Carnavorn Gorge	Ar-Ar	30.7 ± 0.5
Waltenburg (2006)	Carnavorn Gorge	Ar-Ar	27.4 ± 1.0
Cohen et al. (2007)	The Steeple	Ar-Ar	27.3 ± 0.4
Cohen et al. (2007)	4.5 km East of Mt Rugged	Ar-Ar	27.7 ± 0.4
Cohen et al. (2007)	3.4 km South-West of Mt Rugged	Ar-Ar	27.7 ± 0.5
Cohen et al. (2007)	0.5 km South-West of Mt Black	Ar-Ar	29.6 ± 0.5
Sutherland et al. (2012)	Mt Yanalah	K-Ar	29.9 ± 3.4

Al_2O_3, Na_2O, and TiO_2 compared to other lavas with similar silica content in the province. The upper section of the second episode was described as a trachybasalt, consistent with a fractionated version of the lower unit (Waltenburg, 2006).

A handful of studies have collected and described xenoliths from Buckland, and these provide a more direct way to describe the lithospheric mantle beneath the volcanic province (Skae, 1998). Griffin et al. (1987) described two spinel lherzolite samples from Buckland in a large central-east Queensland xenolith dataset. Compared to worldwide averages, Buckland xenoliths have greater abundances of Al_2O_3, CaO, Na_2O, MgO, MgO/Mg+Fe, and Cr/Cr+Al. Opx-spinel thermometry was carried out, yielding a temperature of 900-1050 °C, with an estimated pressure of 9-16 kbar (26-50 km). Kennett et al. (2011) places the Moho depth underneath Buckland between 38 – 40 km and (Davies and Rawlinson, 2014) places the lithospheric-asthenospheric boundary (LAB) ~ 125 km placing these xenolith samples in the lowermost crust to lithospheric mantle. Skae (1998) sampled 14 anhydrous xenoliths from Buckland, at Rewan, Battleship Spur, and Mt. Tabor, which were exclusively sampled from basanite hosts. 13 of the samples collected were spinel lherzolites, with mineral proportions of olivine > orthopyroxene > clinopyroxene > spinel. Both Griffin et al. (1987) and Skae (1998) argue the source assemblage of Buckland to be spinel lherzolite.

1.7 Aims

This study aims to investigate and identify the source assemblage for primitive alkali basalts and basanites from Buckland Volcanic Province and the possible role of mantle metasomatism. To do

this, whole rock and olivine minor and trace element chemistry from primitive samples (MgO > 7.5 wt. %) will be combined to indicate minerals present in the source assemblage, and to possibly indicate and identify a metasomatic agent. It is hypothesised the source assemblage for Buckland has undergone metasomatism which has produced phase not typically found in the primitive upper mantle or lithospheric mantle, which will be indicated in either whole rock or olivine chemistry. It is hoped this approach will form preliminary work for a broader investigation into the source assemblages for more eastern Australian intraplate volcanic provinces, and identifying how metasomatism may have altered the lithospheric mantle.

Chapter 2

Methods

2.1 Sample Selection

Fifty-two basalt samples, collected throughout Buckland, were made available for this study by Dr. Kim Jessop, Department of Earth and Planetary Sciences, Macquarie University, Australia. These samples were collected for the Jessop (2012) Master thesis. Twelve primitive samples containing suitable olivines for EPMA and LA-ICP-MS analysis were selected. Whole rock data was available for nine samples (75207, 75222, 75225, 75226, 75235, 75238, 75240, 75242, and 75244) which were filtered for MgO > 7.5 wt. %, while three samples (75115, 75116 and 75119) had no previous data available and were selected based on hand sample identification. Figure 1.5 shows where samples were collected from Buckland volcanic province.

2.2 Petrography

Three 100 μm thick sections were made at Macquarie University for samples 75115, 75116, and 75119, and were added to the nine sections already available from Jessop (2012). Individual olivines were selected for EPMA and LA-ICP-MS analysis based on a large enough surface area for a laser ablation spot-size up to 85 μm away from iddingsite alteration, any cracks or fractures, and any crystal heterogeneity.

2.3 Electron probe micro-analyser

For this study, the EPMA was used twice. The first analysis was a preliminary survey to select samples with high Fo mol. % for LA-ICP-MS analysis. The second EPMA analysis spots were measured next to LA-ICP-MS craters for internal standardisation to quantify the LA-ICP-MS results.

Prior to both analyses all thick sections were cleaned, polished, and desiccated to reduce sample contamination and topographic effects on back-scattered electrons. For the second analysis all thin sections were re-cleaned, polished and desiccated to reduced material ejected from the laser ablation

craters during the LA-ICP-MS analysis. For both analyses all thick sections were carbon coated to 20 nm thickness using a Quorum Q150T Turbo-Pumped Carbon Coater. Coated sections were inserted on a thin section slide holder, olivine grains were preselected, and tracked on the thick sections using cross polar images.

EMPA analysis was carried out on a CAMECA SX100, at Macquarie University, Australia. Operating conditions were set to 20 kV acceleration voltage, with a 20 nA electron beam current, a 2 μm beam diameter, on a 3 minute 40 second measuring time per run. The WSD with long count times to acquired major elements Mg, Fe, and Si and minor elements Al, Ca, Cr, Mn, and Ni (Table 2.1). Points were pre-selected during petrographic analysis to best represent the unaltered chemistry the olivines, see Section 2.2 Petrography for more details.

Table 2.1: Wavelength dispersive spectrometer (WDS) element conditions for quantitative analysis of olivine major and minor element compositions for EPMA. SCO, San Carlos Olivine

Element	**Mg**	**Al**	**Si**	**Ca**	**Cr**	**Mn**	**Fe**	**Ni**
WDS Channel	4	4	2	1	1	5	5	3
WDS Crystal	TAP	TAP	TAP	LPET	LPET	LLIF	LLIF	LLIF
Line	Kα	Kα	Kα	Kα	Kα	Kα	Kα	Kα
Standard	SCO	Al_2O_3	SCO	$CaSiO_3$	Cr_2O_3	Mn garnet	Fe_2O_3	Ni
Measuring time (s)	40	80	60	60	60	80	40	120
Detection limit (ppm)	90	30	60	40	50	80	120	54

2.4 Laser ablation - inductively coupled plasma - mass spectrometry

Concentrations of ^{7}Li, ^{11}B, ^{23}Na, ^{24}Mg, ^{25}Mg, ^{26}Mg, ^{27}Al, ^{29}Si, ^{30}Si, ^{31}P, ^{43}Ca, ^{44}Ca, ^{45}Sc, ^{47}Ti, ^{49}Ti, ^{51}V, ^{53}Cr, ^{55}Mn, ^{59}Co, ^{60}Ni, ^{62}Ni, ^{63}Cu, ^{66}Zn, ^{67}Zn ^{88}Sr, ^{89}Y, ^{90}Zr, ^{93}Nb, ^{135}Ba, ^{137}Ba, ^{139}La, ^{140}Ce, ^{157}Gd, and ^{172}Yb were measured using an Aligent 7700cx Quadrupole LA-ICP-MS, at Macquarie University. This study used a 193 nm ArF excimer laser for the laser ablation introduction system, and argon was used as a carrier gas. The total count time for each analysis was 180s, which included a 120s background, and a 60s dwell time for 600 laser shots at 10 Hz with a fluence of 5 J/cm^2. National Institue of Standards and Technology (NIST) 612 and 610 glasses (Jochum et al., 2011), BCR-2G (Jochum et al., 2007), and San Carlos Olivine (Batanova et al., 2015), were used as standard reference materials with recommended GeoReM values (http://georem.mpch-mainz.gwdg.de/start.asp?dataversion=current), and ^{29}Si, measured as Si by EPMA,

was used as an internal standard. The laser spot size was 85 μm, or occasionally 65 μm if an olivine was too small, the larger spot was too close to cracks, zonation boundaries, or iddingsite alteration.

2.4.1 Interference Corrections and Data Reduction

There are two main types of interferences when using LA-ICP-MS, which are polyatomic and isobaric interferences. Polyatomic interferences are avoided by careful selection isotopes which do not have overlap. However isobaric interferences on ^{45}Sc, ^{63}Cu, ^{66}Zn and ^{67}Zn are potentially present. Scandium is a monoisotopic element, with an interference from $^{29}Si^{16}O$, which needs correction. Foley et al. (2011) and De Hoog et al. (2010) corrected for $^{29}Si^{16}O$ interference on ^{45}Sc by measuring ^{43}Ca and ^{44}Ca, ^{44}Ca is interfered by $^{28}Si^{16}O$, assuming ^{28}Si and ^{29}Si natural isotopic ratios apply, the amount of $^{29}Si^{16}O$ interference on ^{45}Sc can be inferred. This was applied to this study with no success. However since Si is a major element in olivine and obeys olivine stoichiometry, and $^{28}Si/^{29}Si$ obey natural isotopic proportions, interference values should be consistent between studies. This is seen in the literature De Hoog et al. (2010) calculated an interference of 0.2 ppm of $^{29}Si^{16}O$ on ^{45}Sc, and Foley et al. (2011) calculated an interference of 0.25 ppm. This study uses the correction calculated by Foley et al. (2011) for $^{29}Si^{16}O$ interference on ^{45}Sc of 0.25 ppm. ^{63}Cu is interfered by $^{23}Na^{40}Ar$, which is no issue considering the low concentration of Na in olivine, however using NIST 612 for standardisation may be an issue since it contains 14 wt. % Na_2O. To navigate this issue, an extra data reduction run was made to standardise ^{63}Cu using BCR-2G, which only contains 3.6 wt. % Na_2O (Foley et al., 2011). Foley et al. (2011) found the interference for BCR-2G was negligible, and fell below the 2-sigma error of the measurement for ^{63}Cu. ^{66}Zn may be interfered by $^{26}Mg^{40}Ar$, whereas ^{67}Zn only has an abundance of 4% and an interference from $^{27}Al^{40}Ar$, which provides a similar situation for $^{23}Na^{40}Ar$ on ^{63}Cu. (De Hoog et al., 2010) showed ^{66}Zn had limited $^{26}Mg^{40}Ar$ production in the plasma, and Foley et al. (2011), showed a rate of production between ^{66}Zn and ^{67}Zn that only differed by 0.5%. The astonishingly similar rate of production of ^{66}Zn and ^{67}Zn, very limited interference of ^{27}Al, and limited argide production in the plasma, led to ^{66}Zn being used in this study since it has a higher natural isotope abundance. Data reduction was carried out using the Glitter^{TM} software package (Griffin et al., 2008). Homogeneous sections of signal were selected in Glitter^{TM} to control for inclusions, and fractionation variables down the laser ablation hole on the olivine grain. Results of replicate measurements on NIST 612 and BCR-2G compared to preferred GeoRem values are given on Table 1 in the Appendix. All NIST612 average values fall within 1SD of GeoRem values. Most individual outlier values that fall outside 1SD of GeoRem values align when the 1SD of the

measurement is taken into account apart from a single ^{90}Zr measurement. All measurements for ^{63}Cu fall within 1SD for BCR-2G.

2.5 X-ray florescence (XRF)

Sample fractions between 2-10 mm, leftover from thin section block cuttings were powdered in an tungsten carbide mill in preparation to make glass discs for XRF analysis. The volatile content was determined by the weight loss-on-ignition at 1100°C. Glass discs were prepared in a platinum crucible with a flux of 12:22 lithium borate:lithium metaborate. Each sample was place in a rocking furnace for 20 minutes at 1050°C. Analysis was carried out using a PANalytical Axios WDXRF, at Macquaire University, using the U.S.G.S. Hawaiian Basalt BHVO-2 as a standard reference material.

2.6 Solution – inductively coupled plasma – mass spectrometry (ICP-MS)

Whole-rock digestions for solution ICP-MS analysis were prepared using the following method: 0.1 g of sample powder was weighed into clean 15 mL Savillex Teflon beakers and the mass recorded to four decimal places. Samples were digested using a 1:1 mixture of concentrated HF (Merck, Suprapur grade) and singly distilled concentrated HNO_3 (Merck, Analar grade) at 150°C for 24 hours, then dried down and repeated. This step was followed by adding 2 mL of perchloric acid $HClO_4$ (Merck Suprapur) and refluxing at 170°C. The prechloric acid solution was then dried down at 150°C, 170°C, and then 190°C to remove any fluorides that may have formed. A few millilitres of 6N HCl was added and dried down at 190°C to remove any residual perchloric acid left in the sample. Finally, 6N HNO_3 was added and heated at 150°C for 24 hours, which was not allowed to fully dry and then made up in 10 mL of 2% HNO_3 and 0.25% HF. Each sample solution was diluted with up to 100 mL with 2% HNO_3 and 0.25% HF. 5.0 mL of each sample solution was spiked with 0.02 mL of a ^{6}Li, As, Rh, In, Tm and Bi solution in order to correct for instrument drift during analysis. The spiked samples were run on an Agilent 7500cs quadrupole ICP-MS at Macquarie GeoAnalytical at Macquarie University, Earth and Planetary Sciences. The calibration standard used was BCR-2. 1:1000 and 1:5000 spiked solutions of standards BIR-1, BHVO-2, and BCR-2 were run throughout the day as a check for accuracy and checked against reported values along with blanks of HNO_3.

Chapter 3

Results

3.1 Petrographic observations

Petrographic analysis was carried out for all 12 samples. Table 3.1 summarises general petrographic observations of each selected sample, Figure 3.1 and 3.2 show representative slides. The majority of samples used in this study were fresh, with little to no alteration. Some samples show significant alteration of olivine to iddingsite and some minor groundmass alteration, with 75226 being the most severe. Olivine phenocryst are typically subhedral to anhedral, however some larger grains in the basanites are subhedral to euhedral and are assumed to be xenocrysts. Most olivines have rims visible in birefringence, with minor to no reaction rims.

Table 3.1: Petrographic descriptions of thick section observations. Rock type is based on the total alkali vs. silica (TAS) classification scheme of Le Maitre et al. (2004), see Figure 3.1.

Sample #	Rock type	Texture	Phenocryst	Groundmass	Comments
75115	Basanite	porphyritic	ol, opx, cpx	ol, cpx, opx, ne, ox	Bimodal ol phenocrysts
75116	Basanite	porphyritic	ol, opx, cpx	plg, ne, ox	some ol is fragments of larger grains
75119	Basanite	porphyritic	ol, cpx	ol, cpx, ox	Bimodal ol phenocrysts. Altered groundmass.
75207	Alkali Basalt	trachytic	ol	ol, cpx, plg, fs, mag, il, ap, ox	Alteration of ol to idd. Spi inclusions in ol.
75222	Basanite	porphyritic	ol, opx, cpx	ol, cpx, ne, mag, pal	Amygdules present. Possible ol, cpx, and plg xeno.
75225	Basanite	porphyritic	ol	ol, cpx, ne, mag, pal, ap	Large >500μm mag grains. Some ol alteration to idd.
75226	Basanite	porphyritic	ol, plg	ol, cpx, plg, mag, py	Most oli is altered to idd.
75235	Basanite	porphyritic	ol, opx, cpx	ol, cpx, mag, glass, pal	Clusters of ol and cpx, maybe small xenoliths.
75238	Basanite	porphyritic	ol	ol, cpx, plg, il	Bimodal size of ol phenocrysts, possibly xeno.
75240	Alkali Basalt	trachytic	ol, cpx, plg	ol, cpx, plg, fs, mt, il	Ol phenocrysts show strong zoning in biofringence.
75242	Basanite	porphyritic	ol, opx, cpx	ol, opx, cpx, plg, mt, ap, glass	Amygdales present.
75244	Basanite	porphyritic	ol, opx, cpx	ol, opx, cpx, mt, ap, ne, glass	Some alteration of ol to idd.

ol = olivine; opx = orthopyroxene; cpx = clinopyroxene; plg = plagioclase; spi = spinel, ap = apatite; fs = feldspar; mt = magnetite; pal= palygorskite; ox = oxide; ne = nepheline; idd = iddingsite; il; ilmenite; py = pyrite; xeno = xenocryst.

3.2 Whole rock chemistry

3.2.1 Major elements (Figure 3.3 & 3.4a-i)

Major element data for the whole rock samples is given in Table 3.2, and displayed in Figures 3.3 and 3.4. Figure 3.3 is a total-alkali vs. silica diagram, a useful tool to characterise basalts, which classifies samples 75207 and 75240 as alkali basalts, while all other samples are classified as basanites.

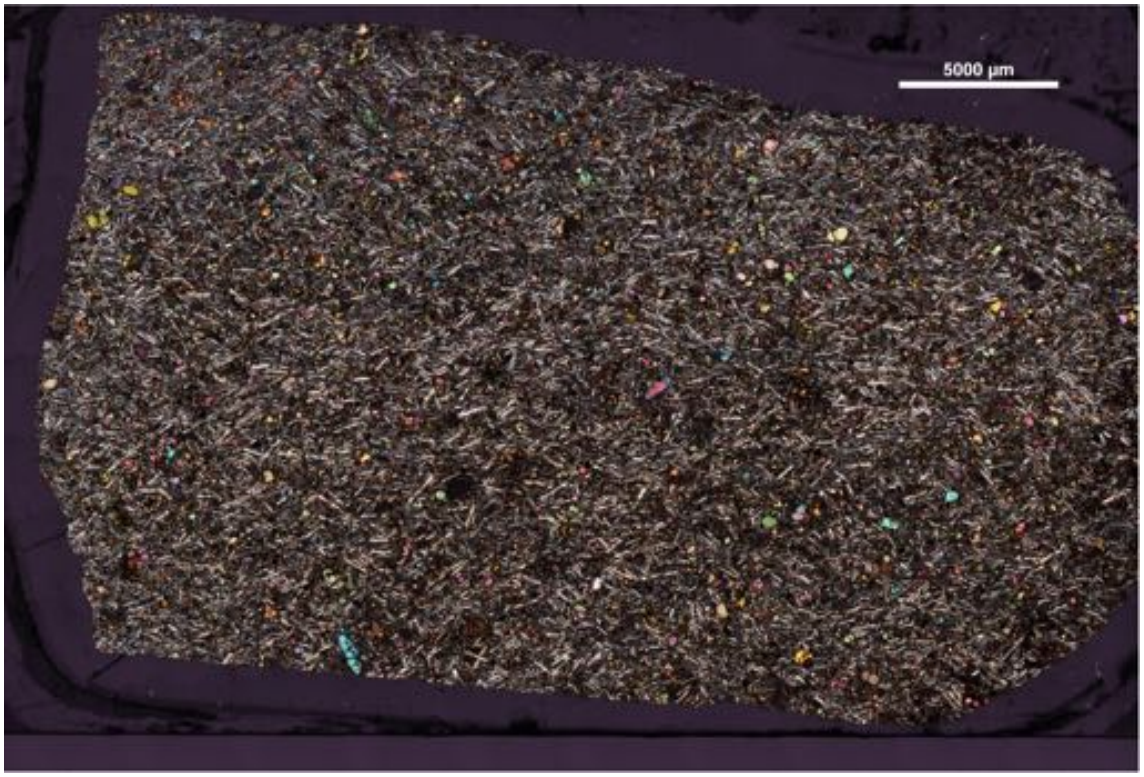

Figure 3.1: A representative thin section of the alkali basalts. Sample is 75240, refer to Table 3.1 for a description.

Figure 3.2: A representative thin section of the basanites. Sample is 75244, refer to Table 3.1 for a description.

Figure 3.4a-i shows alkali basalts contain lower K_2O, MnO, P_2O_5, FeO, and TiO_2, and contain higher SiO_2, and Al_2O_3 than the basanites. Distinct negative trends are seen in SiO_2, Al_2O_3 compared to MgO, with other trends possible in other oxides, but natural variation and limited sampling seems to convolute any other observable trends.

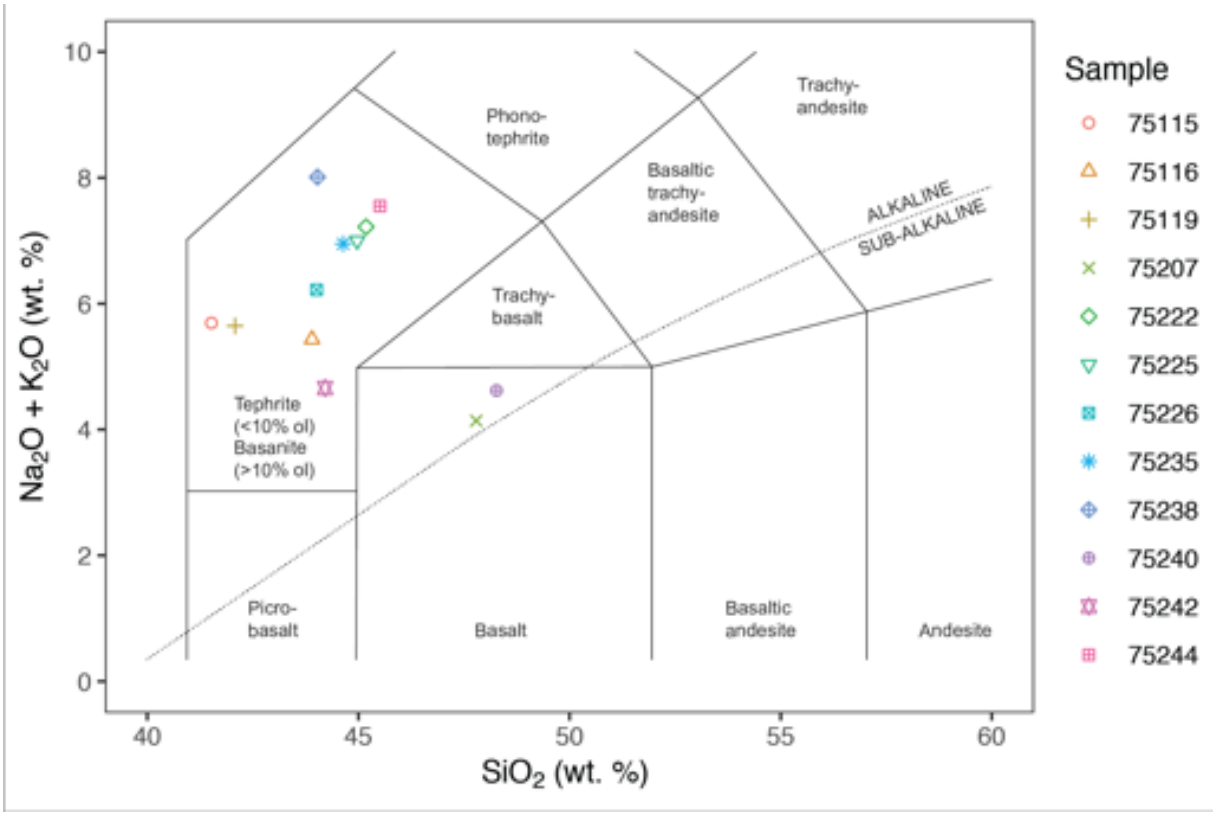

Figure 3.3: A TAS diagram of whole rock data. 75207 and 75240 both plot as alkali basalts, while all other samples plot as basanites. 75115, 75116, and 75119 are from this study, with all other data collated from (Jessop, 2012). Fields from Le Maitre et al. (2004) and Irvine and Baragar (1971).

3.2.2 Minor and trace elements (Figure 3.5)

Figure 3.5 shows a incompatible element variation diagram of results from this study (75155, 75116, and 75119) and trace element data from (Jessop, 2012). The two alkali basalt samples 75207 and 75240 have less enriched incompatible element signatures compared to those of the basanites. 75244, and 75115 show relative similar enrichments in incompatible elements, with the only discernible difference being 75115 does not have a P depletion; however, 75115 has a similar compatible element pattern to the alkali basalts, whereas 75244 has similar compatible element pattern to the basanites. Compared to the basanites, the alkali basalts are depleted in incompatible elements. Basanites, excluding 75115, have OIB-like trace element patterns, with peaks at Nb and Ta, and gradually decreasing in normalised patterns towards Rb and Yb (Sun and McDonough, 1989). Samples 75207, 75240, and 75115 have incompatible element patterns where there is an increase from Th to Rb. Common depletions are seen in K, Pb, P (except for 75115), and Ti (except for 75207).

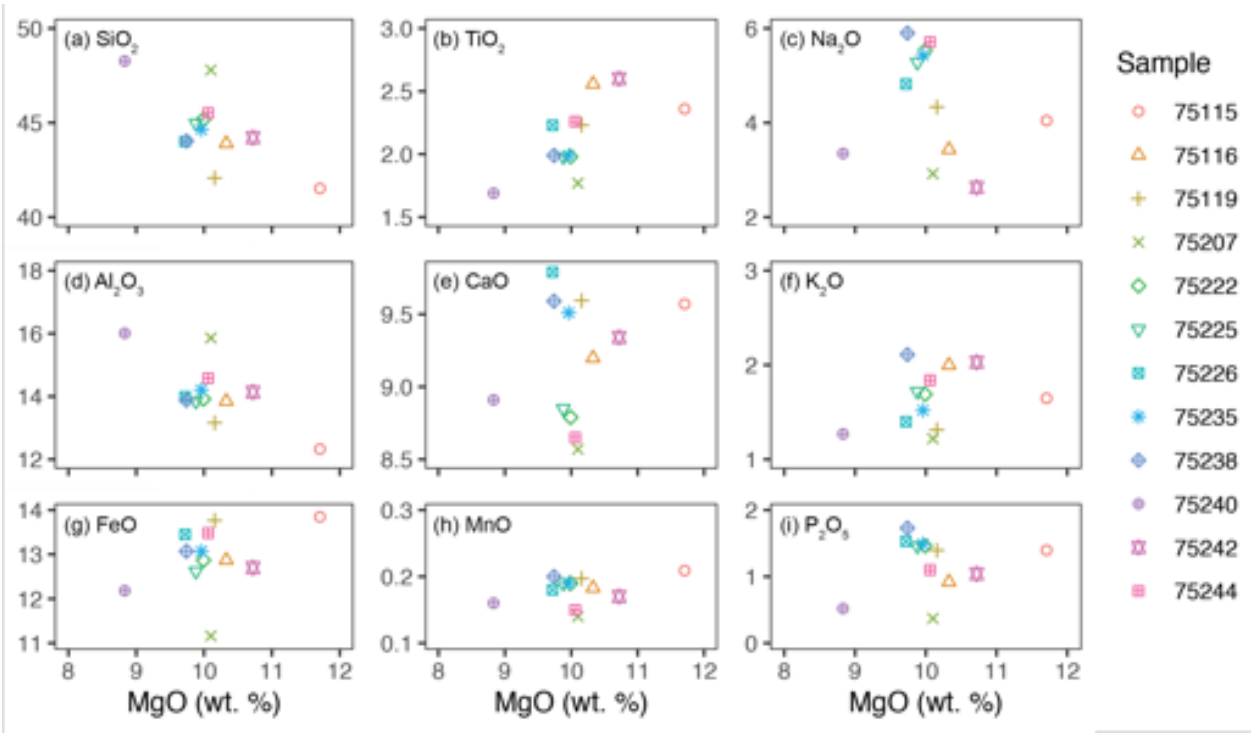

Figure 3.4: MgO vs. major element data, with all measurements in wt. %. 75115, 75116, and 75119 are from this study, with all other data collated from (Jessop, 2012).

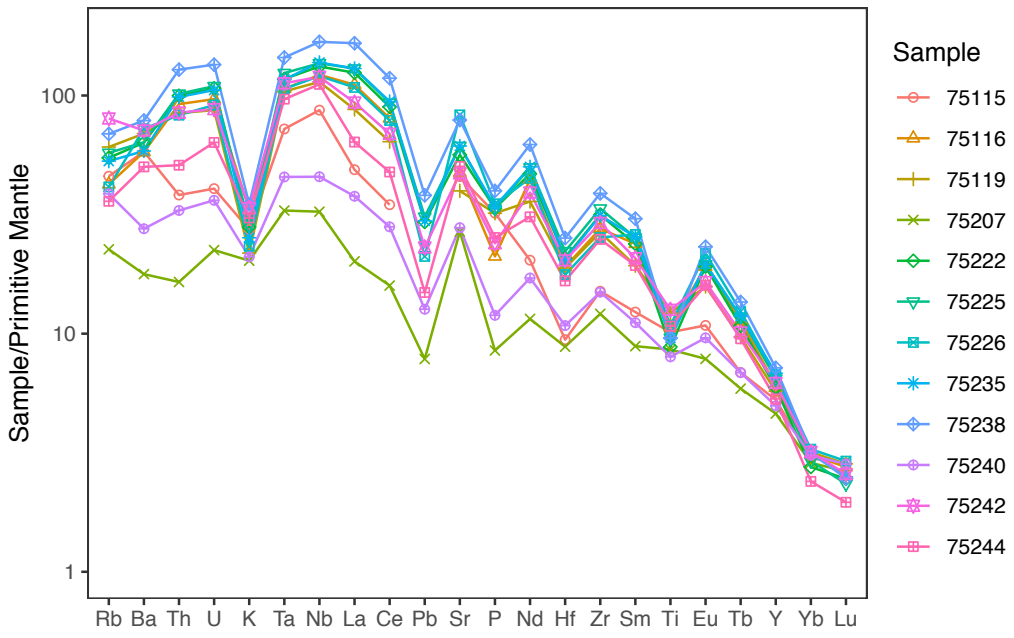

Figure 3.5: Incompatible element variation diagram of whole rock analyses. 75115, 75116, and 75119 are from this study, with all other data collated from (Jessop, 2012), showing whole rock trace element variations for all samples olivine was analysed from. 75207 and 75240 are alkaline basalts and all other samples are basanites.

Table 3.2: Whole rock chemistry data. Major elements in wt.% in oxides and trace elements in ppm.

Sample	75115	75116	75119
SiO_2 (wt.%)	41.52	43.901	42.08
TiO_2	2.36	2.56	2.23
Al_2O_3	12.33	13.85	13.16
Fe_{tot}	13.85	12.87	13.76
MnO	0.21	0.18	0.20
MgO	11.71	10.33	10.16
CaO	9.57	9.20	9.59
Na_2O	4.05	3.43	4.33
K_2O	1.65	2.00	1.31
P_2O_5	1.34	0.92	1.40
LOI	1.11	0.93	1.58
Total	99.74	100.17	99.80
$Mg^{\#}$	64.01	62.80	60.83
Li (ppm)	7.2	6.9	5.9
Be	2.13	3.21	3.05
Sc	24.9	18.1	22.0
Ti	13177	13843	15864
V	207	150	192
Cr	226	289	207
Mn	1413	1431	1348
Co	86.6	92.6	102.2
Ni	217	300	239
Cu	79	57	71
Zn	98	121	141
Ga	17.3	18.8	20.2
Rb	29.1	26.9	38.6
Sr	964	1000	839
Y	24.0	27.6	26.1
Zr	169	309	298
Nb	62	87	81
Mo	2.0	5.1	2.8
Cd	0.08	0.06	0.05
Cs	0.49	0.39	0.33
Ba	406	405	484
La	33.5	76.5	60.1
Ce	61.7	142	114
Pr	7.2	16.0	13.1
Nd	27.3	59.6	48.1
Sm	5.5	10.6	8.6
Eu	1.82	3.21	2.65
Tb	0.74	1.22	1.05
Gd	5.1	8.7	7.3
Dy	3.8	5.5	5.0
Ho	0.72	0.95	0.89
Er	1.91	2.33	2.27
Yb	1.48	1.53	1.57
Lu	0.21	0.20	0.21
Hf	2.92	5.89	5.83
Ta	2.97	4.38	4.27
Th	3.25	7.82	7.17
U	0.85	2.03	1.82

Table 3.3: Due to the 50-page limit of this thesis averaged olivine concentrations are given for each sample. Major elements in wt.% in oxides were by EPMA-WDS; trace elements in ppm by LA-ICP-MS. * represents one measurement above detection limit, so no standard deviation was calculated.

Sample	75207		75240		75115		75116		75119		75222		75225		75226		75235		75238		75242		75244	
Lithology	Alkali Basalt		Alkali Basalt		Basanite		Basanite		Basanite		Basanite		Basanite		Basanite		Basanite		Basanite		Basanite		Basanite	
No. grains	n=9	±2σ	n=10	±2σ	n=10	±2σ	n=9	±2σ	n=10	±2σ	n=9	±2σ	n=6	±2σ	n=7	±2σ	n=3	±2σ	n=10	±2σ	n=9	±2σ	n=9	±2σ
MgO (wt.%)	42.00	4.92	42.48	3.49	48.55	1.11	44.01	5.90	45.93	7.68	44.38	6.95	49.16	0.92	46.01	6.40	45.79	9.90	49.31	1.09	48.60	2.01	46.94	5.28
Al_2O_3	0.04	0.04	0.05	0.01	0.02	0.01	0.06	0.10	0.03	0.05	0.02	0.01	0.01	0.01	0.04	0.13	0.02	0.03	0.01	0.01	0.01	0.01	0.03	0.04
CaO	0.23	0.10	0.22	0.03	0.06	0.06	0.17	0.17	0.12	0.26	0.13	0.29	0.05	0.02	0.09	0.17	0.11	0.22	0.04	0.01	0.05	0.06	0.09	0.01
Cr_2O_3	0.03	0.02	0.04	0.01	0.01	0.03	0.02	0.03	0.01	0.01	0.00	0.01	0.01	0.01	0.01	0.02	0.01	0.02	0.01	0.01	0.01	0.01	0.01	0.02
MnO	0.23	0.10	0.22	0.06	0.15	0.30	0.20	0.08	0.19	0.15	0.25	0.20	0.14	0.03	0.17	0.10	0.20	0.21	0.14	0.05	0.14	0.03	0.15	0.06
FeO_{tot}	16.87	5.85	16.28	3.75	9.88	1.32	15.14	7.37	12.65	8.59	14.32	7.73	9.26	0.85	12.22	6.86	12.63	11.67	9.29	1.23	9.78	2.51	11.27	6.08
NiO	0.25	0.12	0.27	0.07	0.38	0.04	0.26	0.17	0.35	0.18	0.30	0.14	0.39	0.02	0.33	0.13	0.32	0.20	0.39	0.03	0.38	0.05	0.35	0.10
SiO_2	39.10	0.94	39.28	0.87	40.65	0.36	39.66	1.39	40.15	1.82	39.71	1.58	40.92	0.26	40.14	1.41	39.93	2.63	40.88	0.48	40.71	0.57	40.48	1.40
Total	98.75	0.67	98.82	0.69	99.69	0.91	99.51	0.69	99.41	0.73	99.10	0.59	99.93	0.34	99.01	0.93	99.02	0.72	100.06	0.65	99.68	0.29	99.32	0.63
M site	1.995	0.007	1.993	0.007	2.001	0.008	1.999	0.011	1.996	0.004	1.997	0.008	1.999	0.008	1.992	0.011	1.998	0.012	2.003	0.007	1.999	0.006	1.990	0.011
T site	1.005	0.004	1.006	0.004	1.001	0.004	1.002	0.005	1.004	0.003	1.004	0.005	1.002	0.004	1.005	0.006	1.003	0.004	1.000	0.003	1.002	0.003	1.006	0.005
Total	2.999	0.003	2.998	0.003	3.002	0.004	3.001	0.006	3.000	0.002	3.001	0.004	3.001	0.004	2.998	0.005	3.001	0.008	3.003	0.004	3.001	0.003	2.996	0.006
Fo	81.56	7.10	82.28	4.60	89.75	1.41	83.76	8.35	86.49	10.12	84.57	9.21	90.44	0.96	86.95	8.04	86.46	13.50	90.44	1.40	89.85	2.74	88.08	6.98
Li (ppm)	4.47	2.76	4.13	1.65	2.84	1.95	2.51	0.81	3.55	2.37	4.93	1.47	3.70	1.90	3.12	2.07	3.47	2.04	4.28	2.71	2.85	1.92	2.94	1.36
B	6.15	2.94	5.57	0.71	8.84	1.66	6.12	2.34	4.84	0.45	5.28	1.37	4.19	0.66	3.49	0.83	3.36	0.87	5.77	2.04	4.81	0.64	5.90	1.52
Na	111	214	99.2	31.2	55.3	86.7	87.4	65.2	91.3	138	52.05	50.4	33.97	38.6	64.64	58	45.13	33.4	27.62	30.6	49.56	48.7	80.65	93.0
Al	194	129	220	38.0	94.6	289	222	252	121	227	56	60.8	47.5	20.0	88.12	124	63.0	37.0	44.3	28.7	68.2	47.8	165	233
P	94.6	29.4	152	70.3	56.7	46.0	126	132	90.6	180	64.0	80.4	40.9	19.9	79.8	110	40.3	49.3	30.3	14.7	47.8	37.3	75.6	59.5
Ca	1467	553	1431	223	338	435	1177	1139	515	850	361	574	251	96.1	534	754	321	272	216	54.8	271	273	1013	1416
Sc	6.16	2.16	5.17	0.71	3.66	0.87	4.43	2.08	2.98	1.41	2.36	0.56	2.46	0.42	2.70	1.25	2.50	0.15	2.82	0.52	2.50	0.69	3.07	1.08
Ti	69.7	48.3	71.2	7.8	15.7	21.3	77.2	81.0	37.1	70.4	16.5	21.7	13.5	10.6	25.2	48.8	20.7	23.5	9.5	9.1	9.4	11.1	38.3	70.1
V	14.38	6.88	9.49	0.87	2.43	2.39	6.41	4.79	3.11	4.18	1.58	0.47	1.98	1.09	2.88	2.20	2.93	0.68	1.97	0.73	2.56	2.53	3.67	4.41
Cr	272	125	249	26.9	68.5	167	138	120	58.5	90.2	29.1	24.1	41.2	38.6	65.2	79.8	51.6	15.3	43.2	39.9	56.0	52.8	74.3	115
Mn	1992	564	1803	342	1216	220	1667	640	1437	670	1878	1065	1212	171	1425	623	1337	417	1228	377	1238	228	1333	289
Co	188	9.28	188	4.1	152	5.3	185	40	166	31.8	158	15.5	152	1.5	158	22.1	155	8.2	150	6.3	157	18.7	163	26.1
Ni	1941	722	2154	476	3013	266	2111	1349	2843	1033	2539	934	3097	164	2776	800	2870	469	3058	362	3046	363	2903	685
Cu	2.08	1.37	2.01	1.27	1.87	1.79	1.86	0.70	1.41	0.57	1.65	0.44	1.21	0.64	1.62	1.30	1.35	0.39	1.23	0.80	1.48	1.40	1.34	1.04
Zn	192	50	177	56	72	54	145	107	107	129	170	100	73	42	115	99	84	90	64	66	72	69	105	118
Ga	0.231	0.142	0.235	0.051	0.068	0.166	0.173	0.167	0.102	0.161	0.066	0.039	0.059	0.029	0.097	0.138	0.094	0.079	0.046	0.041	0.048	0.040	0.155	0.284
Sr	0.319	1.249	0.363	0.793	0.613	2.160	0.476	1.093	0.726	2.602	0.564	1.427	0.061	0.184	0.585	1.492	0.215	0.639	0.170	0.544	0.302	1.352	0.854	1.680
Y	0.154	0.091	0.135	0.044	0.032	0.049	0.097	0.095	0.059	0.093	0.089	0.152	0.026	0.017	0.050	0.088	0.037	0.023	0.023	0.025	0.028	0.042	0.046	0.056
Zr	0.357	0.754	0.672	3.140	0.220	0.596	0.347	1.071	0.177	0.646	0.183	0.487	0.389	0.825	0.225	0.878	0.331	0.925	2.555	13.69	0.015	0.011	0.857	2.769
Nb	0.012	0.026	0.010	0.014	0.128	0.495	0.232	1.014	0.046	0.195	0.023	0.066	0.010	0.020	0.013	0.032	0.013	0.028	0.027	0.042	0.005	0.008	0.055	0.135
Ba	0.087	0.110	0.354	1.102	0.394	1.001	0.080	0.098	0.560	1.852	0.185	0.501	0.049	0.044	0.300	0.652	0.079	0.125	0.262	0.502	0.053	0.068	0.275	0.749
La	0.007	0.001	0.035	0.097	0.022	0.073	0.046	0.068	0.075	0.216	0.023	0.043	0.012	0.006	0.019	0.029	0.015	0.017	0.034	0.072	0.034	0.079	0.015	0.019
Ce	0.028	0.098	0.035	0.086	0.036	0.140	0.015	0.026	0.111	0.378	0.030	0.070	0.016	0.017	0.021	0.047	0.022	0.031	0.040	0.145	0.161	0.623	0.040	0.097
Gd	0.029	0.014	>0.007	0.002	0.018	*	0.025	*	0.044	*	>0.006	0.004	>0.005	0.002	>0.007	0.007	>0.006	0.002	>0.111	0.016	>0.005	0.002	0.025	0.014
Yb	0.042	0.029	0.044	0.039	0.016	0.006	0.026	0.009	0.020	0.011	0.022	0.026	0.020	0.017	0.023	0.016	0.018	0.008	0.025	0.010	0.021	0.015	0.024	0.019

3.3 Olivine chemistry

Averaged olivine chemical data for each sample are given in Table 3.3. For clarity, olivine results have been divided into their host rock type; alkali basalt, basanite (see Figure 3.3 for TAS classification), or peridotite xenocrysts. Peridotitic xenocrysts are classified using minor element criteria from Bussweiler et al. (2017). Olivine grains are considered xenocrysts with Fo ≥90, Ni ≥ ~2350 ppm, Mn ≥ ~1160 ppm, Mn ≥ ~750 ppm.

There are notable differences in the results, with higher values, up to ~ 100 ppm, for LA-ICP-MS values compared to EPMA. This is well explained by Fritschle et al. (2013) who noted higher Cr and Ba concentrations in LA-ICP-MS on phlogopite using the two techniques. This difference is due to the different spatial resolution of the two measurements. EMPA analyses are only about 2 μm in size, whereas LA-ICP-MS craters are much wider and have a much greater vertical extension. Results presented here will use minor and trace elements obtained from LA-ICP-MS for consistency.

3.3.1 Major and minor elements (Figure 3.6, 3.7a-f, 3.8a-d, & 3.9)

The Fo content of the basanite olivine phenocrysts range between $Fo_{91–75}$, with a mean of Fo_{87}, alkali basalts have a range of $Fo_{86–73}$, with a lower mean of Fo_{82}, and xenocrysts range between $Fo_{91–90}$, with a mean of Fo_{91}. SiO_2 shows a positive linear correlation with Fo content (Figure 3.6), with an $R^2 = 0.97$.

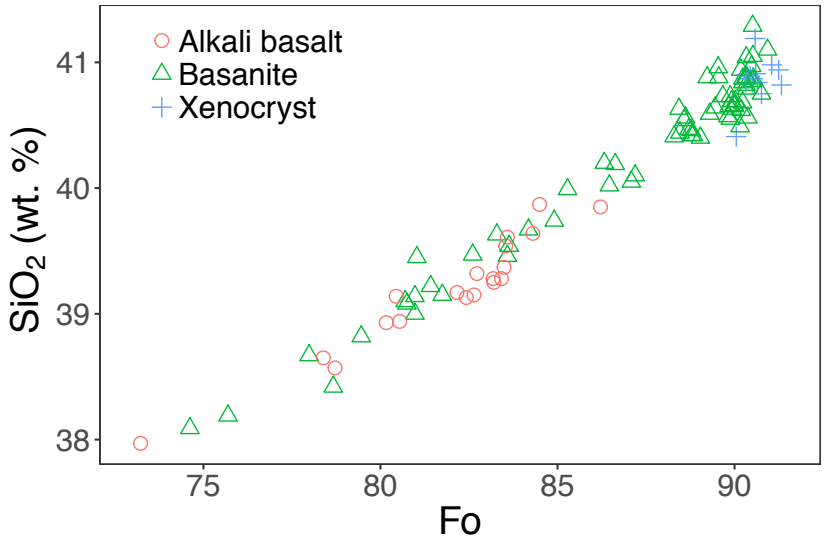

Figure 3.6: A bivariate plot showing SiO_2 (wt. %) against Fo. Si is structural component of olivine which is shown by the almost linear ($R_2 = 0.97$) correlation with Fo.

Figure 3.7a-f shows a core-to-rim line analysis of Fo, Ni, Si, and Ca, on an olivine grain from

75115. This shows remarkable homogeneity in the core of the phenocryst. Ca line shows some random high peaks in an otherwise low concentration phenocryst core, which may be interpreted as zoning or a heterogeneous core. However, these peaks are from surface contamination, seen in Figure 3.7b which shows spots of dust approximately in same location as peaks on the Ca line profile. Fo shows a uniform core with a step like feature towards the rim.

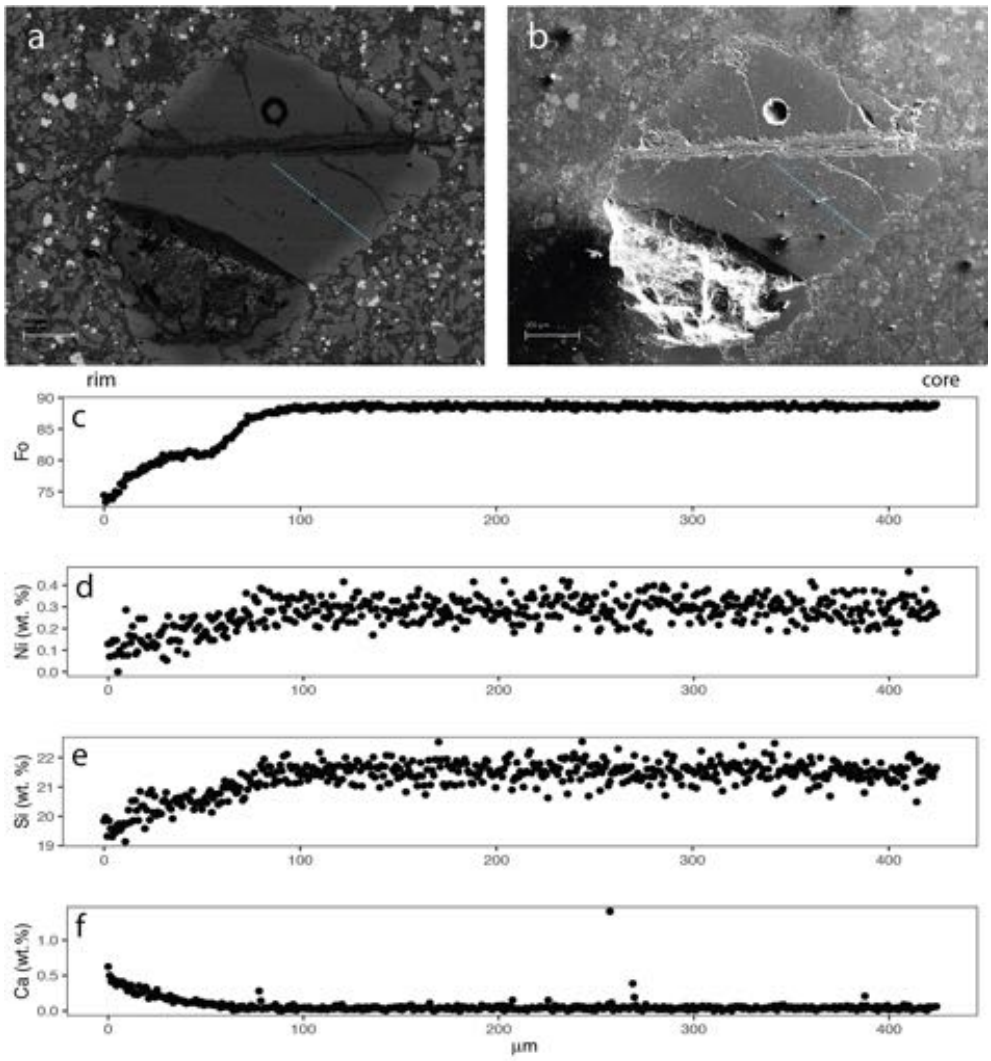

Figure 3.7: A line profile of a representative olivine phenocryst (sample 75115) from the Buckland Volcanic Province. (a) an electron backscattered image showing zoning, and a dashed blue line were profile was taken; (b) a secondary electron image, showing relief where dust and other material contaminated the sample surface, high spikes in Ca occur where relief is seen on the sample surface, so these high peaks are interpreted as sample contamination and should be disregarded. (c) the Fo content of the olivine, which shows a homogeneous core, and a step like fractionation trend. The step is likely a phenocryst overgrowth on a xenocryst core; (d) Ni (wt. %) content; (e) Si (wt. %) content;, and (f) Ca (wt. %) content. Error for the measurements were taken before and after the profile was measured, MgO ±0.2 (wt. %), FeO ±0.1 (wt. %), NiO ±0.01 (wt. %), CaO ±0.01 (wt. %), SiO ±0.13 (wt. %) Images a, and b, and the line profile measurements were obtained with a CAMECA SX100 EPMA, at Macquaire University.

Figure 3.8a-d shows quantitative elemental maps of Fe (Figure 3.7a), Ca (Figure 3.7b), Mg (Figure 3.7c), and Si (Figure 3.7d). Fe, and Ca show low concentrations in the core, that increase towards the

rim of the grain. Conversely, Mg, and Si show high concentrations in the core, and low concentrations towards the rim on the grain. Fe concentrations become particularly low closer to the cracks, and Ca, Si, and Mg all have sharp increases in composition on the cracks.

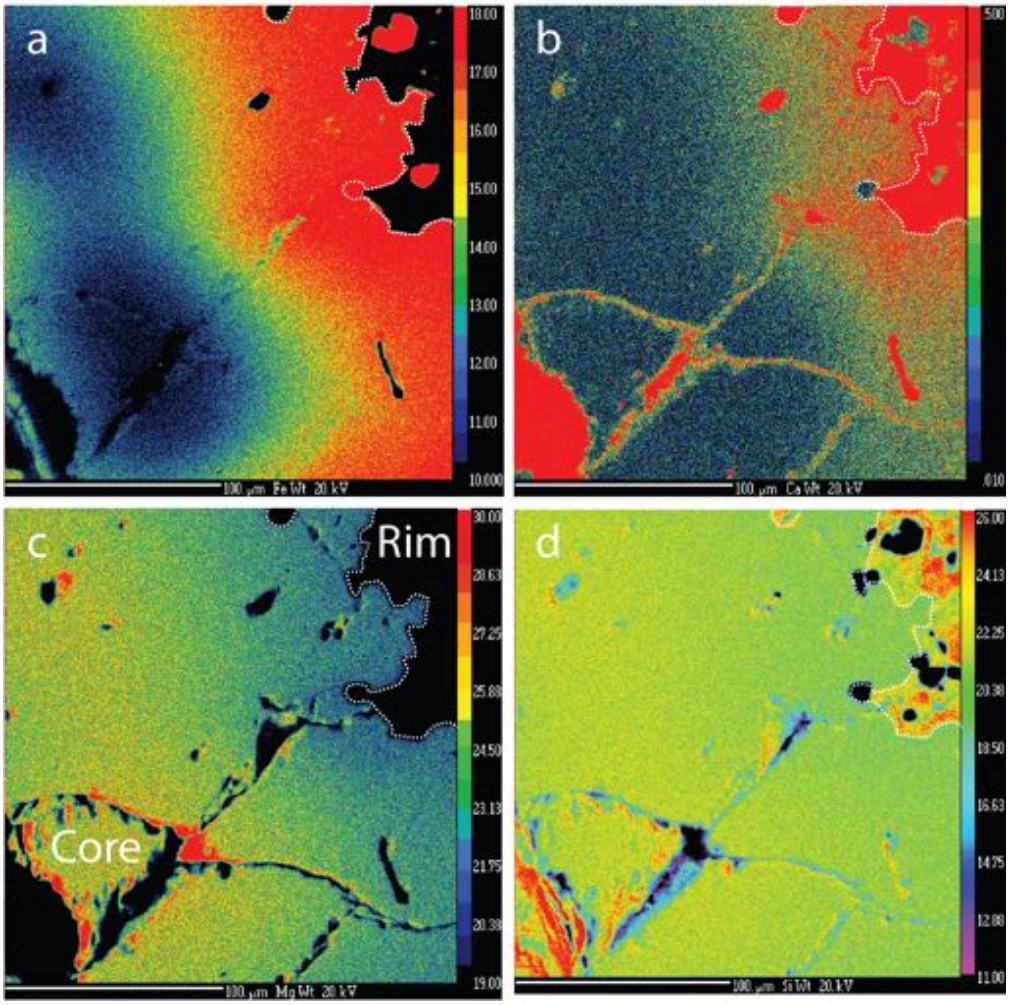

Figure 3.8: A quantitative elemental map showing distributions of Fe wt. % (a), Ca wt. % (b), Mg wt. % (c), and Si wt. % (d). Measurements obtained with a CAMECA SX100 EPMA, at Macquaire University. Core and rim of the olivine grain labelled in Figure 3.6c, with the rim outlined in a white dashed line in each image.

Ca is the only element outside of the first row transition elements present in minor element concentrations. Figure 3.9 plots minor elements against Fo from potential peridotite xenocrysts, and phenocrysts from the alkali basalts, and basanites. Xenocrysts, which have a narrow Fo range ($Fo_{91–90}$), have a narrow range of concentration, and low Ca concentrations (374 - 179 ppm), that scatter close together. Alkali basalts, have a larger range of Ca concentration (838 - 1700 ppm), at lower Fo contents than the xenocrysts. The basanites have two populations of Ca, separated by Fo content, $Fo_{91–88}$ and $Fo_{87–73}$. The $Fo_{91–88}$ population has the largest range (142 - 2321 ppm), while the $Fo_{87–73}$ range has a narrower range (151 - 1848 ppm).

Mn, Co, and Ni are first row transition metals present in minor element concentrations. These

elements are also plotted against Fo in Figure 3.9. Mn and Co have negative correlations with Fo, while Ni is positively correlated with Fo. Xenocrysts have small ranges for Mn (1071 - 1157 ppm), Co (146 -156 ppm), and Ni (3020 - 3223 ppm). Alkali basalt phenocrysts have a large range for Mn (1477 - 2429 ppm), and Ni (1482 - 2549 ppm), while Co (182 - 197 ppm) has a narrow range. Basanite phenocrysts have the largest ranges with Mn (1151 - 3080 ppm), Co (142 - 208 ppm), and Ni (1402 - 3292 ppm). The mean of each transition element is also different for each classification, xenocrysts have the lowest mean for Mn and Co , and the highest mean for Ni (3138 ppm). Alkali basalt olivines have the highest mean for Mn (1892 ppm) and Co (188 ppm), and the lowest mean for Ni (2050 ppm). The basanite olivines have a lower mean of Mn (1460 ppm) and Co (162 ppm) than the alkali basalts, but a much higher mode for Ni (2753 ppm) than alkali basalt olivines.

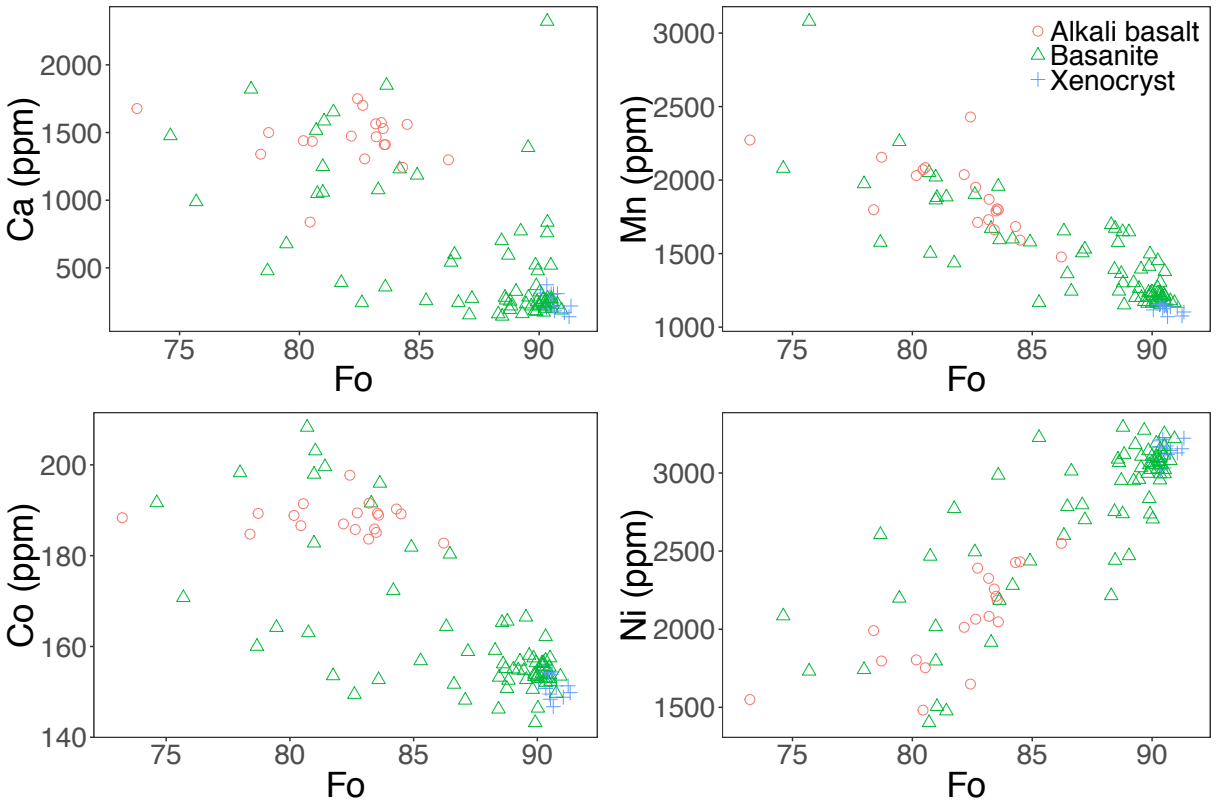

Figure 3.9: Olivine minor elements plotted against Fo concentration.

3.3.2 Trace elements (Figures 3.10 - 3.15)

Trace, and ultra trace element abundances in Buckland olivines are described here in terms of their range, and mean, and the concentrations are compared to compared to their Fo mol. %. Two Fo groups will be described here, the high Fo group, $Fo_{87.5–92}$, and the low Fo group $Fo_{<87.5}$. Averaged sample concentrations are given in Table 3.3, and individual grain concentrations are given in the appendix.

Non metals

B and P are non-metals present in detectable trace element concentrations in Buckland olivines. B has a similar range for all olivine classifications, with the largest ranges of concentration seen in xenocrysts (4.1 - 10.6), then basanites (2.9 - 9.5 ppm), and then alkali basalts (5 - 9.8 ppm), however each group has similar means (xenocrysts (6.3 ppm), alkali basalts (5.8 ppm), and basanites (5.4 ppm)). P has much larger differences in between each group, xenocrysts (24.4 - 56.6 ppm), alkali basalts (73.6 - 219.4 ppm), and basanites (21.3 - 333.7 ppm), which is also seen in large differences in the mean for P, xenocrysts (36.8 ppm), alkali basalts (124.9 ppm), and basanites (73.6 ppm). Both xenocrysts and basanites have a consistent scattering of olivines over a large range in the high Fo group for B. While the concentrations of P in the high olivine are low, and closely scattered. While the low Fo group has a lower range, with alkali basalts having a higher average concentration of B than basanites.

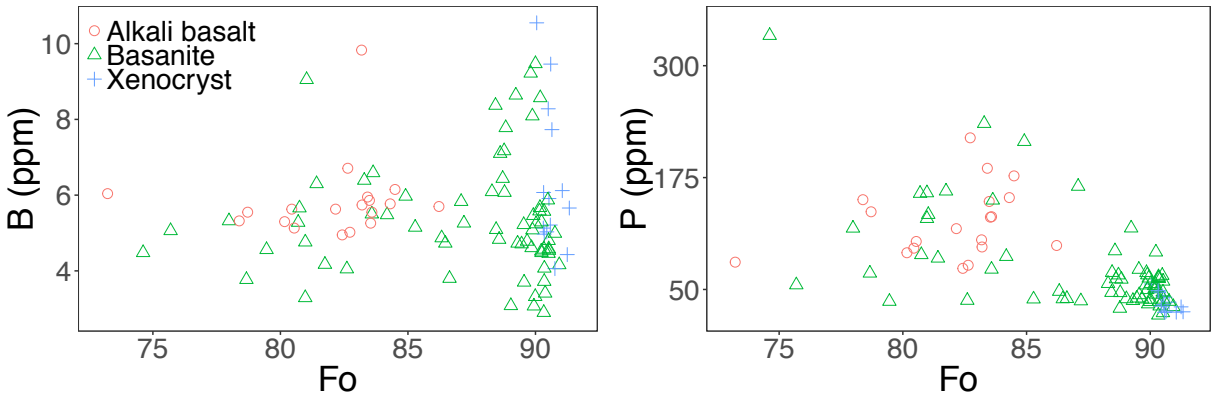

Figure 3.10: Non metals B and P concentrations plotted against Fo concentration for Buckland olivines.

Alkali & alkali earth metals

Li, Na, Sr, and Ba are detectable trace elements present in the Buckland olivines. Figure 3.11 plots Li, Na, Sr, and Ba concentrations against Fo for Buckland olivines. Alkali basalts have the highest mean concentration for Na (55 ppm), followed by xenoliths at (11 ppm), and then basanites (6.93), these elements have a large range compared to other alkali and alkali earth metals. Li concentrations are consistent among each classification, xenocrysts show the smallest range (1.63 - 5.52 ppm), followed by alkali basalts (2.49 - 6.46 ppm), and basanites have the largest range (1.82 - 6.46 ppm). However, alkali basalts have the largest mean (4.3 ppm), followed by basanites (3.5 ppm), and xenocrysts have the lowest mean (3.2 ppm). Sr and Ba have much larger differences between the classifications. Sr has a large range in basanites (1.82 - 6.46 ppm) and the largest mean (0.543 ppm), alkali basalts have a smaller range (0.14 - 1.86 ppm), and a smaller mean (0.341 ppm), and xenocrysts have the

smallest range, below the mean (0.017 - 0.278), with the smallest mean (0.115 ppm). Ba has low concentrations with 47 grains measured below detection limit, most measurements below detection were in the alkali basalts. The mean between each classification is consistent (xenocrysts, 0.200 ppm); alkali basalts, 0.221, however after removing an outlier the mean falls to 0.097; and basanites, 0.224), although the ranges differ between each classification (xenocrysts, 0.023 - 0.65 ppm; alkali basalts, 0.026 - 1.33 ppm, however after removing an outlier the upper limit of the range falls to 0.026 - 0.24; and basanites, 0.019 - 1.94 ppm). Sr, and Ba each have large, consistently scattered trend in the high Fo group. While the low Fo group has lower for Sr, and Ba concentrations. While Li has an almost random scatter for all groups.

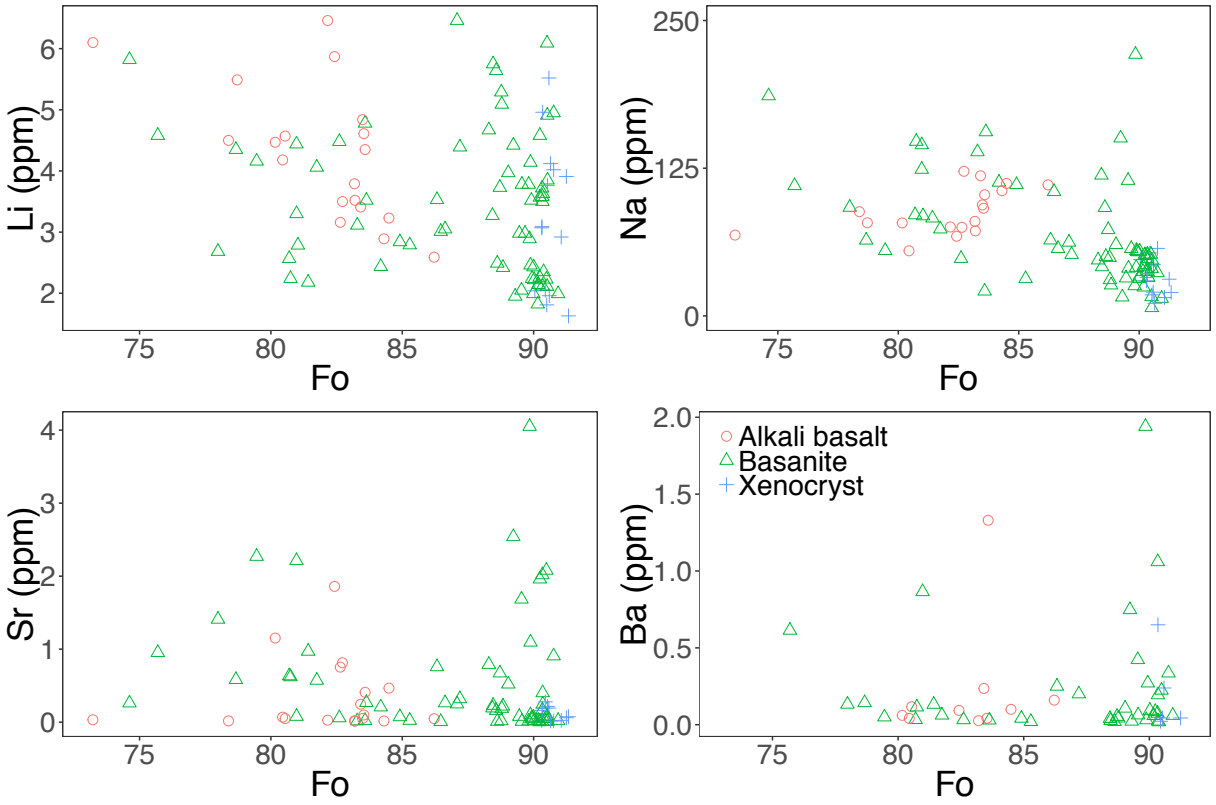

Figure 3.11: Alkali metal & alkali earth metals Li, Sr, and Ba concentrations plotted against Fo concentration for Buckland olivines.

Transition metals

First row transition metals Sc, Ti, V, Cu, and Zn are all present in trace element concentrations in Buckland olivines. Element has similar proportions for each olivine classification group with the high in the alkali basalts > basanites > xenocrysts. Zn has the highest concentrations for each classification, followed by Ti, V, Sc, and Cu. Titanium has the highest ranges (xenocrysts, 4.15 - 23.75 ppm; alkali

basalts, 7.41 - 89.61 ppm; basanites 1.17 - 112.65 ppm). The >50 ppm group is a mixture of basanite and alkali basalt olivines, while the <50 ppm group is almost all, aside from one alkali basalt olivine, basanite olivines. The high Fo group shows a scatted trend of basanite, and xenocryst olivines between 0 and 50 ppm. Zinc has the highest mean values in each group, with the highest concentrations in the low Fo group. Zn has a negative correlation, in both basanite and alkali basalt olivines, with Fo in the low Fo group, while there is a scatter between 40 - 140 ppm in the high Fo group of both basanite and xenocryst olivines. Scandium and vanadium behave similarly for the low Fo group. Alkali basalts contains higher V and Sc concentrations than the basanites. The high Fo group has a small range of concentrations for V in the xenocryst and basanites olivines, while Sc has a relatively similar range for basanites and xenocrysts compared to low Fo basanites. Copper has the smallest concentrations, but the high Fo basanite olivines have a larger range than the low Fo olivines, with xenocrysts in the high Fo showing similar scatter to the basanites in the low Fo group. The low Fo alkali basalts, and basanites overlap ranges, with the alkali basalts showing slightly higher concentrations.

Second row transition metals all have ultra trace element concentrations in Buckland olivines, and are shown in Figure 3.13. Yttrium mean proportions for each classification are the same as first row transition elements, alkali basalts > basanites > xenocrysts. However, zirconium and niobium mean proportions are different to the rest of the transition metals. Y has a negative correlation with Fo in the low Fo group, with concentrations higher in the alkali basalts than basanite olivines. Niobium has similar ranges for xenocrysts (0.002 - 0.037 ppm), and alkali basalts (0.003 - 0.031 ppm), while basanites are marginally higher (0.002 - 1.14, however after taking out an outlier, the upper limit of the range fell to 0.002 - 0.5 ppm). The higher range for Nb in basanites is due to some olivines in the high Fo group with high concentrations. Zr concentrations for basanite and xenocryst olivines have large ranges in the high Fo group, while the low Fo group olivines have a smaller ranges, with alkali basalts, and basanites classification overlapping.

Post transition metals

Post transition elements Al, and Ga were detected in trace (Al), and ultra trace (Ga) concentrations, shown in Figure 3.14. Both, Al and Ga mean proportions behaviour similarly between each classification, with Al means roughly an order of magnitude more concentrated in Buckland olivines than Ga. Xenocrysts have the lowest means (Al, 53.7 ppm; Ga, 0.046 ppm), followed by basanites (Al, 111 ppm; Ga, 0.100 ppm), and alkali basalts have the largest concentrations (Al, 208 ppm; Ga, 0.233 ppm). The similar means are also reflected in similar ranges for each classification (Al - xenocrysts,

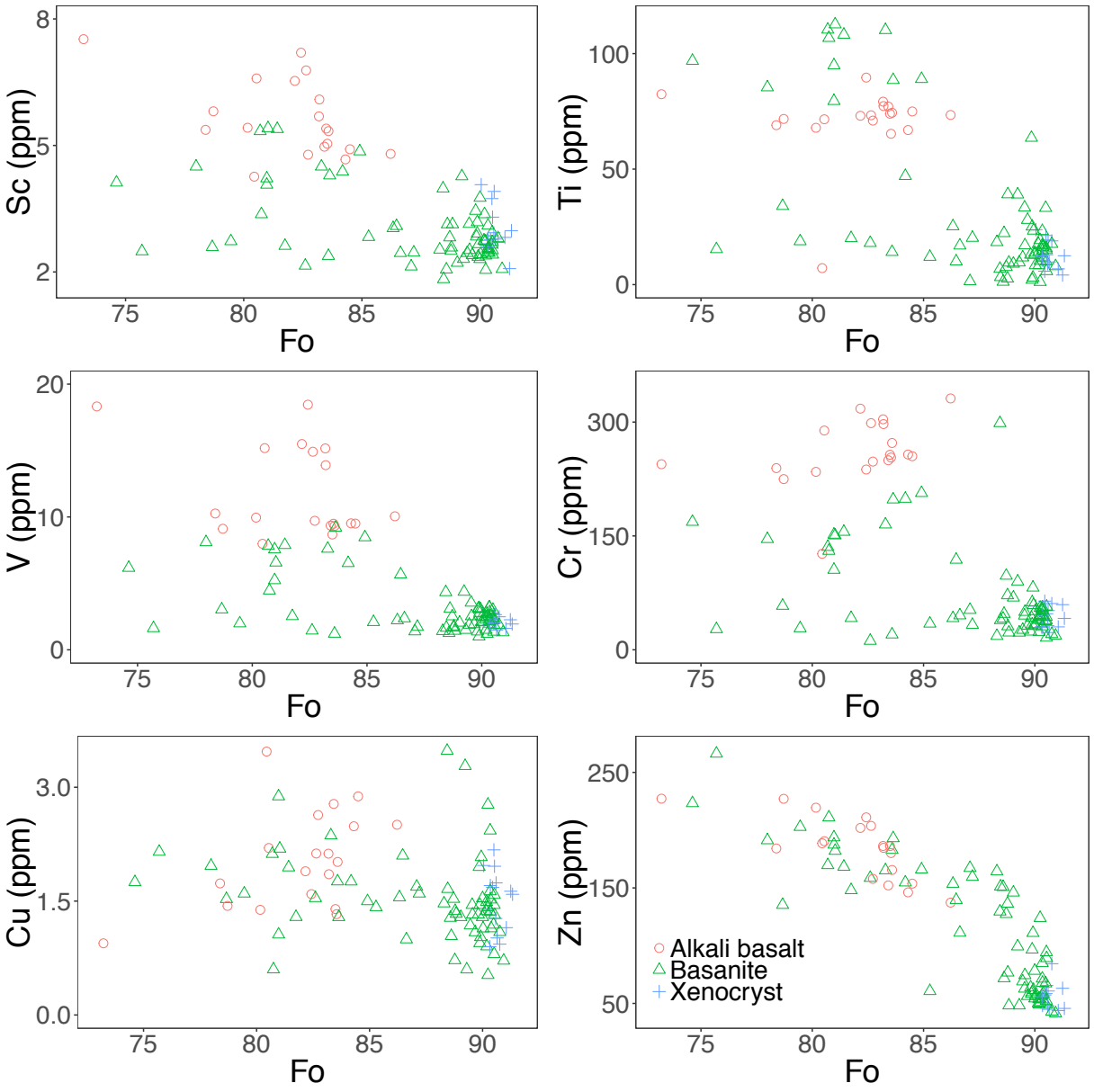

Figure 3.12: First row transition metals Sc, Ti, V, Cr, Cu, and Zn concentrations plotted against Fo concentration for Buckland olivines.

29.4 - 80.7 ppm; alkali basalts, 35.0 - 262 ppm; and basanites 27.4 - 502 ppm; Ga - xenocrysts, 0.018 - 0.086 ppm; alkali basalts - 0.06 - 0.312 ppm; and basanites 0.020 - 0.465 ppm). Both Al, and Ga behave similarly when plotted against Fo. The high Fo group have ultra trace concentrations, however a few basanite olivines Al and Ga concentrations comparatively higher than other olivines with similar Fo. For the low Fo group, two groups are present, a low Al and Ga concentration group is present, mostly of basanite olivines, and a higher concentration group split between alkali basalt and basanite olivines.

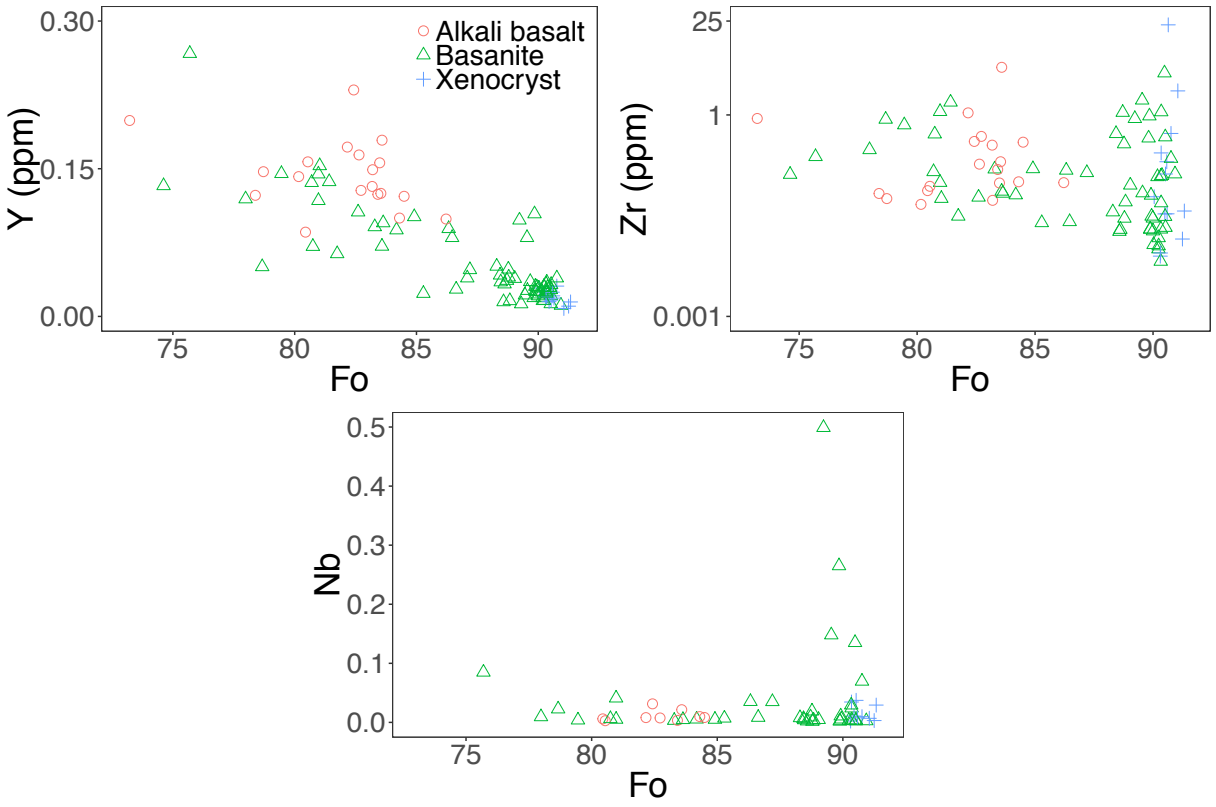

Figure 3.13: Second row transition metals Y, Zr, and Nb concentrations plotted against Fo concentration for Buckland olivines. Note the Zr is plotted on a logarithmic axis.

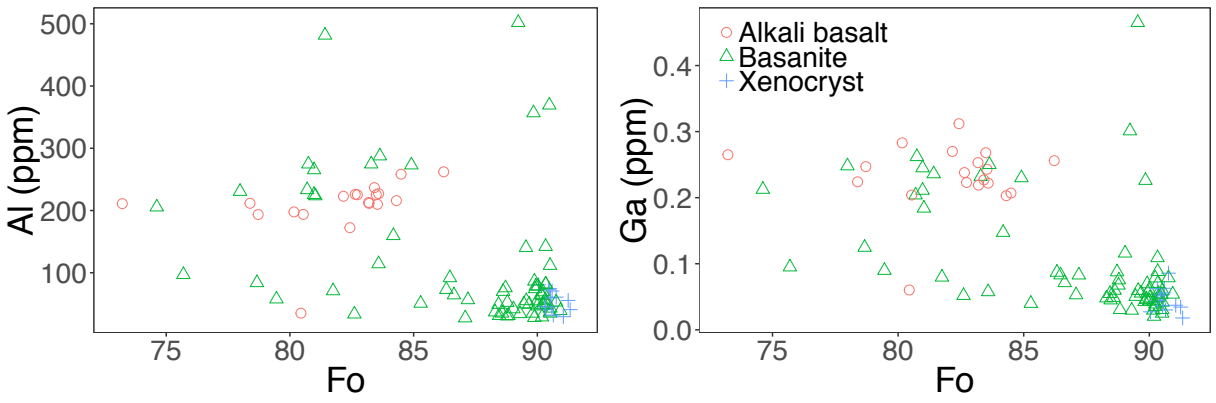

Figure 3.14: Post transition metals Al, and Ga concentrations plotted against Fo concentration for Buckland olivines.

Rare earth elements

Rare earth elements are restricted to ultra trace abundances. La, Ce, and Yb were detectable in the majority of the olivines, however Gd was only detected in 8 of 101 olivine grains, with only one measurement on the xenocrysts for Gd of 0.018 ppm. Basanites have the highest mean for La (0.029 ppm), and Ce (0.030 ppm), Gd (0.030 ppm) whereas the alkali basalts have the highest mean for Yb (0.043 ppm). Ranges vary widely, with the largest ranges in La (xenocrysts, 0.003 - 0.029 ppm; alkali

basalts, 0.003 - 0.107 ppm; basanites, 0.003 - 0.199 ppm), then Ce (xenocrysts, 0.003 - 0.032 ppm; alkali basalts, 0.004 - 0.035 ppm; basanites, 0.002 - 0.628 ppm), then Yb (xenocrysts 0.012 - 0.023 ppm; alkali basalts, 0.019 - 0.084 ppm; basanites 0.011 - 0.050 ppm), with Gd having the smallest ranges (alkali basalts, 0.020 - 0.035 ppm; basanites, 0.021 - 0.044 ppm). However, the ranges for Gd are less reliable since they are close to detection limit, and only have 8 values spread across three classifications. La, and Ce are more concentrated in the high Fo olivines, and are restricted to lower concentrations in the low Fo group (aside from a few La outliers in the low Fo group.) Yb has a small range, but comparatively has lower concentrations in the high Fo group, than the low Fo group.

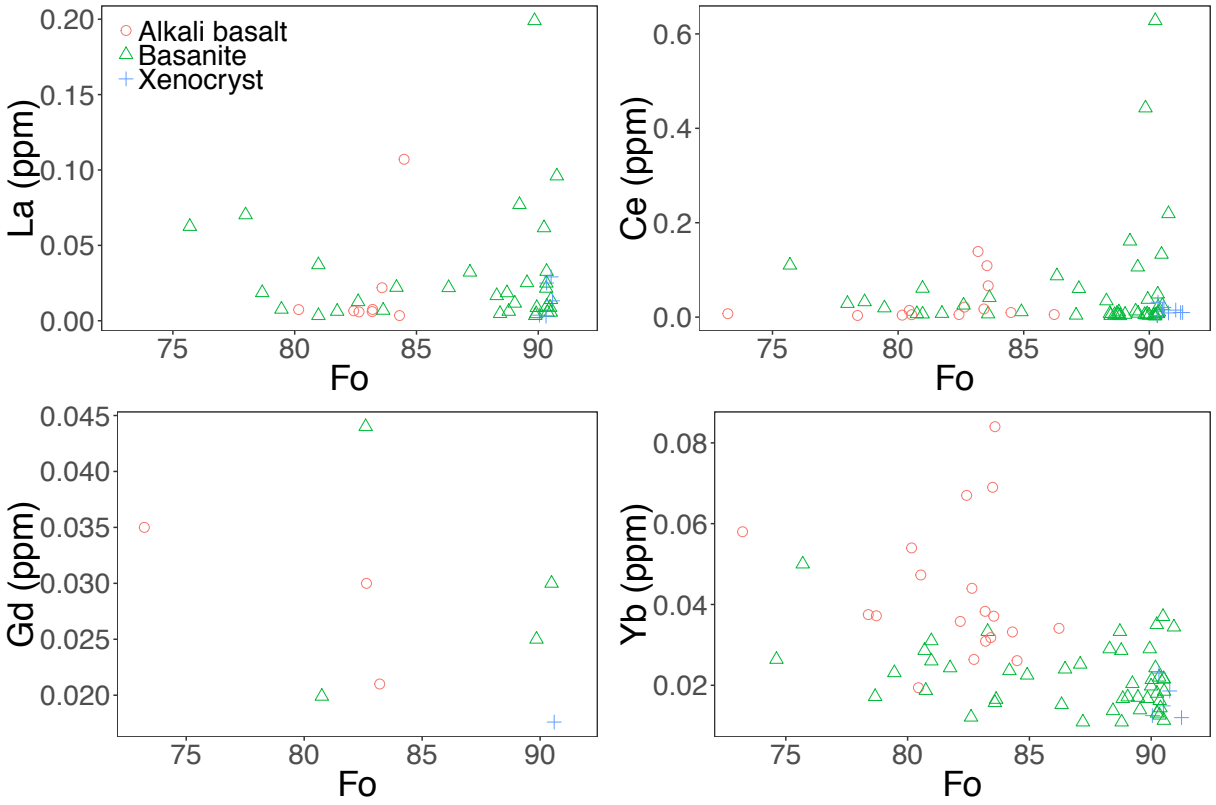

Figure 3.15: Rare earth elements La, Ce, Gd, and Yb concentrations plotted against Fo concentration for Buckland olivines.

Chapter 4

Discussion

This section separates plots into either EPMA data or LA-ICP-MS data, unless otherwise stated, and avoids comparing data from the two measurements. Subtle differences are seen between each method, for example EMPA mean for Ni is 2386 ppm, and Ca is 536 ppm, while LA-ICP-MS means for Ni is 2674 ppm, and Ca is 691 ppm. The LA-ICP-MS means is higher by 289 ppm for NI, and 155 ppm for Ca. This is due to the often subtle differences in the spatial resolution of both measurements (Fritschle et al., 2013), and is addressed in Chapter 1.

4.1 Petrogenesis of alkali basalts and basanites

The $Mg^{\#}$ for whole rock data ranges from 60.31 to 65.56, Ni content is high (185-300 ppm), and Cr content is low (110-289 ppm) suggesting these samples are primary melts. Although high Fo olivines ($Fo_{>87.5}$) are too high for the whole rock $Mg^{\#}$, they are entrained in, suggesting a large proportion of high Fo mol. % olivine phenocrysts are xenocrysts, and do not match the xenocryst criteria of Bussweiler et al. (2017). Figure 3.5c in the previous chapter shows a line profile of an olivine phenocryst from sample 75115, which has a remarkably homogeneous core with a high Fo_{89} with a step-like trend, showing this is a phenocryst rim overprinting a xenocryst core. The line profile suggests no significant diffusion has effected the site where the LA crater is for the LA-ICP-MS data, satisfying the xenocryst data has not been significantly altered by diffusion. From a small dataset it is hard to constrain correlations, but slight correlations between TiO_2 and MgO (Figure 3.2b), and the slight correlation and tight clustering of P_2O_5 and MgO (Figure 3.2i), suggest there is no early crystallisation of apatite and Ti-Fe oxides during fractionation. There is no correlation in the Nb/Rb and K/Rb (not shown), the large variation of LREE and large ion lithophile elements between samples suggest there is a somewhat common source for all the magmas with subtle differences. However, olivine phenocryst ($Fo_{<87.5}$) cores represent olivines which have formed in near-primary mantle melts, or soon after fractionation processes occurred and are useful for distinguishing a source assemblage. Also, similar depletions in the whole rock analysis, particularly K, P, Hf, and Ti are consistent across all samples (excluding P for sample 75115, and Pb was not measured for samples 75115, 75116, and

75119), which is likely due to similar mineral occurrences in the source assemblage, however the variation in Pb suggests it is the result of fractionation processes (Figure 3.3).

4.2 Source assemblage indicators

4.2.1 Peridotite component

Peridotite is usually a component of a source assemblage, the amount of peridotite component is hard to constrain without isotope data (Sobolev et al., 2005; Herzberg, 2011), however it is important to identify a peridotite facies for the source assemblage (Veter et al., 2017). De Hoog et al. (2010) and Bussweiler et al. (2017) both analysed olivine trace elements from different peridotite facies to calibrate an Al-in-olivine-thermometer. A subsequent finding of these studies were neat outlines of how to discriminate between xenocryst and phenocryst olivines. Using olivine xenocryst parameters outlined by Bussweiler et al. (2017), and peridotite facies boundaries outlined by De Hoog et al. (2010), Figure 4.1 shows xenocryst olivines plot as spinel lherzolites. There is a minor overlap in the Sc vs. Zr plot to garnet-spinel peridotite facies, however, De Hoog et al. (2010) noted minor overlaps between these boundaries, which are greater than the overlap present here. Bussweiler et al. (2017) also used an Al vs. V bivariate plot to determine a peridotite facies from, but these two variables together were particularly susceptible to metasomatic effects, and was not used for this reason. Olivine trace elements determine the host peridotite to be a spinel lherzolite, so the Al-in-olivine-thermometer could not be applied since it is only calibrated for garnet peridotites. A spinel lherzolite facies for Buckland agrees with the findings from Skae (1998), and agrees with the current consensus that it forms most of the sub-continental lithospheric mantle beneath eastern Australia (Griffin and O'Reilly, 1986; O'Reilly and Griffin, 1987; O'Reilly et al., 1997; Zhang and O'Reilly, 1997).

4.2.2 Non-peridotite components and their origin

Mantle metasomatic agent

Figure 3.3 shows a primitive mantle normalised trace element spider diagram of whole rock chemistry, with notable depletions in Ti, Hf, P, Pb, and K. The Zr/Hf ratios of the Buckland alkali basalts and basanites ranging for 50–57.9, with the alkali basalts both having Zr/Hf 50, and the basanites range between 51.9–57.9, suggesting mantle heterogeneity in the source assemblage. High Zr/Hf $\sim$ 36, and elevated ratios (> 48) along with Ti/Eu depletions in continental intraplate basalts have been shown to

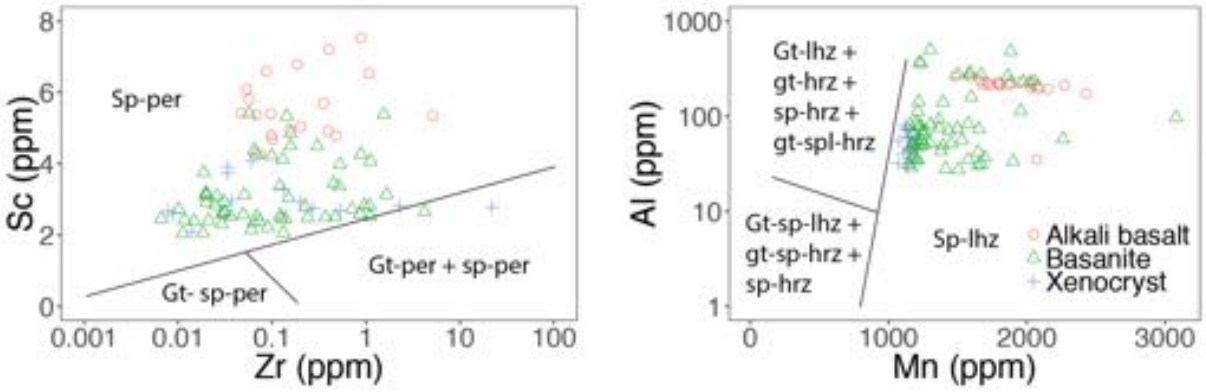

Figure 4.1: Log Zr plotted against Sc, and Mn plotted against log Al. Sp = spinel; gt = garnet; per = peridotite; lhz = lherzolite; and, hrz = harzbergite. Fields reproduced from De Hoog et al. (2010).

be associated with carbonatite metasomatism in the source assemblage (Dupuy et al., 1992; Rudnick, 1994). These could have formed from fractionation effects, but seem to be buffered similarly across all samples suggesting carbonatite metasomatism effects in the source assemblage.

A common measure for low degree partial melts in the mantle is sinusoidal rare-earth element patterns, which has been shown as a way carbonatite melts move through the sub-lithospheric mantle (Navon and Stolper, 1987; Yaxley et al., 1991). Figure 3.13 shows the REE concentrations from Buckland olivines, only La, Ce, Gd, and Yb were measured since most were assumed to be too low to measure in olivine. Gd is mostly present below the detection limit, is assumed to be Gd>Yb, which reflects normal partitioning trends of REE into olivine (Evans et al., 2008; Stead et al., 2017; Taura et al., 1998). Light REE are much more incompatible than heavy REE in olivine (Stead et al., 2017; Taura et al., 1998), however La and Ce both show spikes in concentration in high Fo> 88 greater than Gd and Yb concentrations. La>Ce, but for some olivines Ce>La, and can be described as La>Ce>Yb>Gd or Ce>La>Yb>Gd, which indicates sinusoidal patterns than have been related to chromatographic effects from low degree partial melts (Navon and Stolper, 1987). The grouping of basanite and xenocrysts was based on criteria from Bussweiler et al. (2017), however this can mischaracterise xenocrysts as phenocrysts, especially if they have experienced chromatographic effects (Neumann et al., 2002), so these phenocrysts are likely peridotite xenocrysts. Neumann et al. (2002) argued chromatographic sinusoidal rare earth patterns in peridotite xenocysts are the result of a passing carbonatite melt, which was entrained into the melt.

High Fo–> 87.5 olivines with sinusoidal patterns have low V/Sc indicating the metasomatic agent was present in an oxidised environment (Figure 4.2). The Sc was chosen over Yb to compare to V since Yb is systematically low in the basanites, which may indicate a past garnet signature (Figure 3.13), also Evans et al. (2008) showed that REE partitioning into olivine is greatly decreased in low

silica content in a melt, which is expected for a carbonatite metasomatic agent. The V/Sc is low across all groups, and low (V/Sc => 1) for the high Fo> 88 group, indicating an oxidised carbonatite metasomatic agent, and for the peridotite xenoliths.

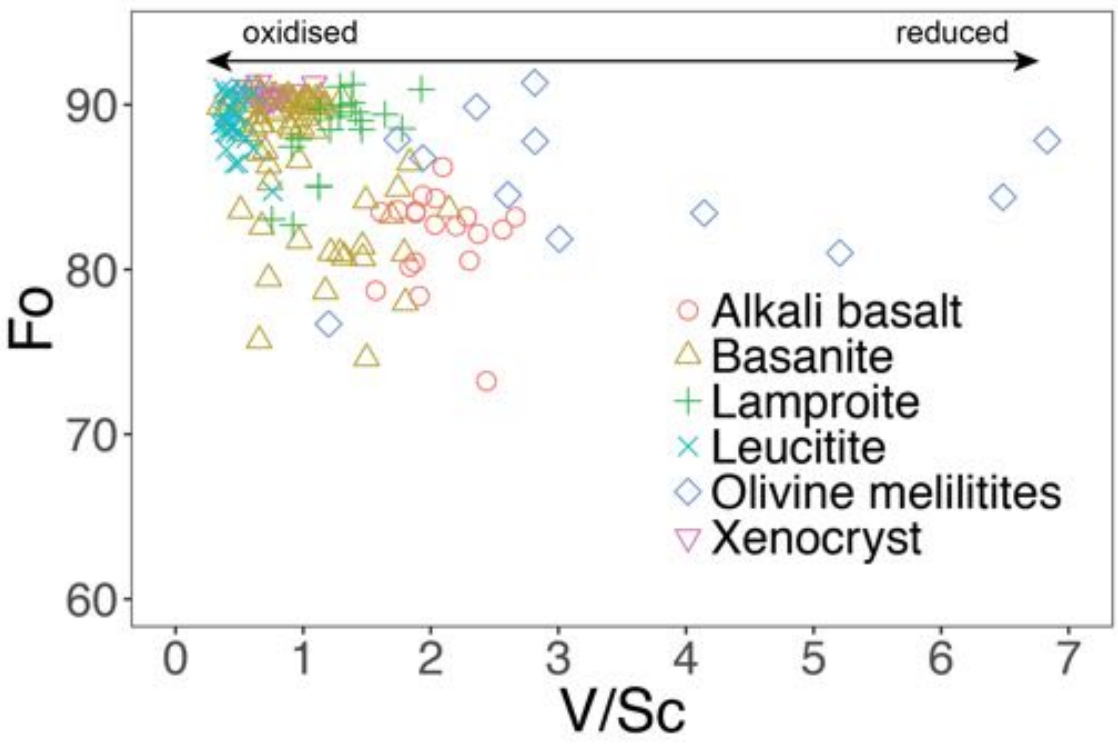

Figure 4.2: Olivine V/Sc plotted against Fo. The arrow at the top show low V/Sc indicates an oxidised setting and high V/Sc indicates a reduced setting. V/Sc data was acquired by LA-ICP-MS, and the Fo content was acquired by EPMA.

Non-peridotite mineral indications

Whole rock K_2O range is restricted (1.22–2.11), and high compared to other eastern Australia basalts (Zhang and O'Reilly, 1997). Figure 3.5 shows an incompatible element variation diagram, and K appears to show a depleted trough for all samples, which is likely buffered by mica (Tappe et al., 2006). Trace elements in olivine have identified phlogopite in non-peridotite source assemblages that have been affected by carbonatite metasomatism (Ammannati et al., 2016; Veter et al., 2017). But phlogopite stability lies between 41 to 96 kbar (Kushiro et al., 1967), which is much deeper than the 16-21 kbar estimates for basanite segregation in eastern Australia (Ewart, 1989). The Mn/Fe and Ni/Mg in olivine is characteristic of phlogopite in the source (Figure 4.3), lending towards the idea phlogopite may be stable at shallower depths (Kushiro et al., 1967). In Figure 4.3, the basanites plot closer towards the red phlogopite star from (Veter et al., 2017), indicating they likely have higher modal phlogopite in the source assemblage. Rosenthal et al. (2009) showed that in a non-peridotite

mantle assemblage containing phlogopite may be stable at depths shallower than 100 km, and as shallow as 70km, leading to the idea phlogopite may be stable in non-peridotite domains within the Buckland source assemblage. If phlogopite is not stable in the Buckland source assemblage, there is the possibility biotite is and gives a mica signature similar to phlogopite. Veter et al. (2017) also suggested phlogopite associated with carbonatite metasomatism is rich in V and Sc, and could scatter the V/Sc of some basanite, and alkali basalt olivines in Figure 4.2 towards a more reduced setting. The V/Sc, and Ni/Mg, and Mn/Fe lend towards the idea of the source assemblage containing high mica, likely a glimmerite.

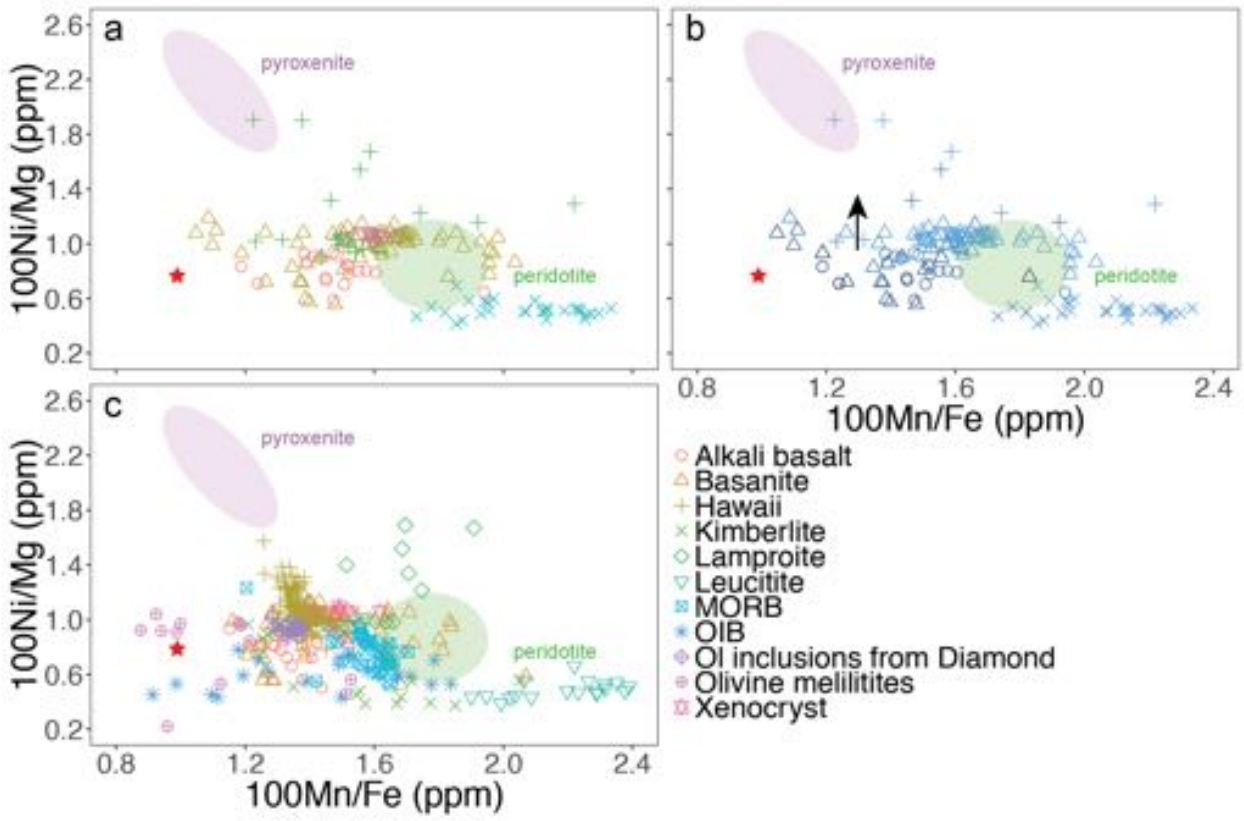

Figure 4.3: Mn/Fe plotted against Ni/Mg to discriminate between peridotite, pyroxenite, and phlogopite source components. The legend for Figure 4.3a can be found on Figure 4.2. Figure 4.3b shares the same shapes as 4.2 and 4.3a, but the shades of blue indicate Fo, ranging from $Fo_{91.33–73.22}$ light blue high Fo and dark blue indicates low Fo. The legend shown is for Figure 4.3c. Mg and Fe, for all plots are EPMA data, Ni and Mn on Figure 4.3a and b are LA-ICP-MS data, and Figure 4.3 Ni and Mn are EPMA data. The purple fields are pyroxenite, the green fields are peridotite from Foley et al. (2013) and Veter et al. (2017). The red star is the average of phlogopite xenocrysts from Mediterranean lamproites from Veter et al. (2017). Fractionation affects Ni/Mg, so the black arrow in Figure 4.3b indicates low Fo olivine would be higher without fractionation effects. The Buckland olivines xenocryst plot just outside the peridotite field, in a similar location to Hawaii. The Buckland alkali basalts, and basanites plot from a depleted peridotite to towards the phlogopite red star, however basanites are closer to the star than the alkali basalts, possibly indicating they have higher phlogopite content. The Ni/Mg trend is high for the Buckland olivines, and moves towards the pyroxenite field, this likely indicates a pyroxene component. Hawaii, and MORB from Sobolev et al. (2007), Ol inclusions in diamond from Sobolev et al. (2009), OIB from Neumann et al. (1999), Kimberlite from , and Lamproite and Olivine meliltite data from Ammannati et al. (2016).

Li is enriched in the crust (30 ± 3.6 ppm) compared to the mantle (~1.5 ppm) (McDonough and

Sun, 1995), with typical peridotite mantle derived olivines containing between 1–2 ppm, pyroxenites up to 3 ppm, and elevated Li in olivine associated with metasomatism (Seitz and Woodland, 2000). Li in Buckland basalts range from 1.63 to 6.46 ppm with Li up to 6.46 ppm in both the alkali basalts and basanites, which overlaps, and significantly exceeds, mantle values (Figure 3.9 in the previous chapter). Post collisional lamproites, from the western Mediterranean olivines have concentrations of Li up to 45 ppm, which was correlated to continental material from whole rock Sr and Li isotope signatures (Prelević et al., 2013; Ammannati et al., 2016). Jaques and Foley (2018) noted, enriched Li in the western Mediterranean is likely preserved since the sources were imbricated together at shallow depths, avoiding interactions with fluids which may have carried Li away. Jaques and Foley (2018) also argued that low Li (~5 ppm; low only compared to the post collisional lamproites that contain Li up to 45 ppm, but still well above the mantle average of 1 – 2 ppm) Li enrichment in olivine was likely higher in the past, and it either diffused back into other mantle domains, or was carried away by passing fluids. However, in the West Kimberley Jaques and Foley (2018) did not able to correlated Pb isotope signatures with continental material. Skae (1998) preformed Pb isotope analysis on basanites from Buckland and reported an HIMU-like arc signature, and elevated Sm and Nd isotope signatures in the alkali basalts, which could be the result of an interaction with a crustal component. It may be possible Li was more concentrated up to 20–30 ppm in the past from subducted continental material and diffused back into the mantle, leaving behind elevated Li concentrations in the source assemblage much lower than those found in the Mediterranean, but still elevated well above mantle values. Figure 4.4 shows Li plotted against Ti and Zn with phlogopite trends from Foley et al. (2013), this figure may indicate that possible continental material has produced mica, possibly biotite or phlogopite agreeing with the V/Sc, Ni/Mg, and Mn/Fe signatures for a glimmerite.

Some elements have partitioning behaviours into olivine that vary with pressure, making it possible for relative pressure estimates between the basanites and alkali basalts. However, some olivines found in the basanites contain low Fo mol. % consistent with the whole rock $Mg^{\#}$, but show minor and trace element signature that significantly overlap with the xenocryst group (Figure 3.12), and are not consistent with elements that have pressure sensitive partitioning behaviours in olivine. Elements known to have high pressure sensitivity partition behaviour include Ca, Na, Cr, V, Sc, Al, Y, and Ti ((see element vs. Fo mol. % bivariate plots in the previous chapter) Brey and Köhler, 1990; O'Reilly et al., 1997; Taura et al., 1998; Beattie et al., 1991). Brey and Köhler (1990) shows lower concentrations of Ca at higher pressures, Taura et al. (1998) shows Na and Al also decrease concentrations with increased pressure. These elements indicated the basanites formed deeper than the alklai basalts, and

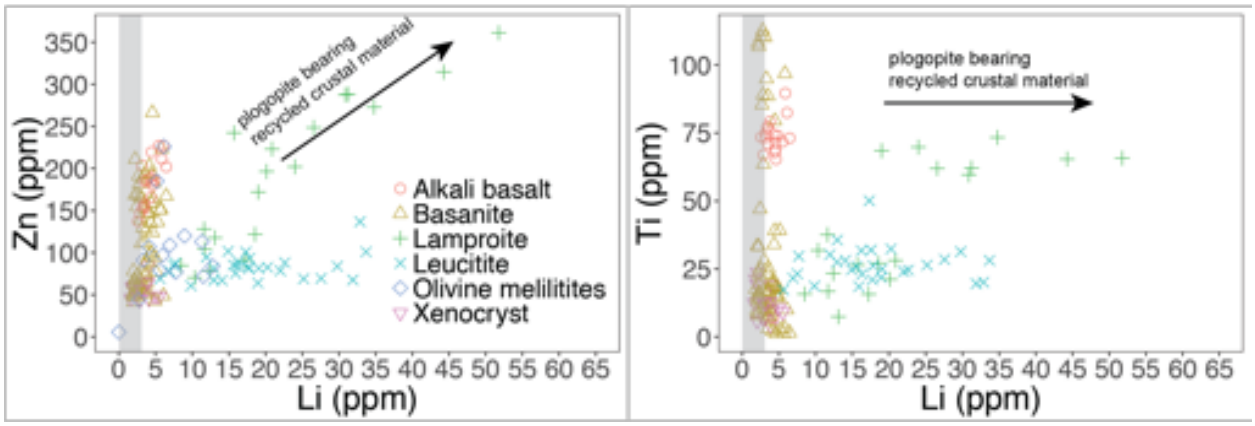

Figure 4.4: Li and Zn, and Li and Ti plotted against each other. The grey band covers peridotite and pyroxentite Li mantle concentrations. All data is from LA-ICP-MS. The alkali basalts, basanites, and xenocrysts are from this study, while lamproite and leucitite data is from (Ammannati et al., 2016), and olivine melilities is from Day et al. (2014). If Li concentrations have diffused back into the mantle, there may be a similar trend to phlogopite from (Foley, 1992), at shallower depths this could be biotite in peridotite, or phlogopite/biotite in non-peridotite domians.

agrees with past literature (Ewart, 1989; Foley, 1992). Melt infiltration, driving metasomatism, may lower the $Mg^{\#}$ of a domain within the lithospheric mantle, which is correlated to lower Fo olivines (Palme and O'Neill, 2014). Due to the depleted nature of this group of olivines, it is possible they are residual xenocrysts of a metasomatised lithospheric mantle domain.

Low Fo olivines show higher concentrations of elements that favour low pressure conditions, indicating they crystallised in a magma chamber closer to the surface (De Hoog et al., 2010; Taura et al., 1998). Particularly, low Fo olivines show high Ni in both alkali basalts and basanite groups. High Ni has been associated with pyroxenite in the source assemblage (Sobolev et al., 2005, 2007), however, these Ni concentrations at lower Fo are similar to mixing trends between pyroxenite and peridotite components calculated by Straub et al. (2008), and unrealistically high for mixing between two peridotite end-members (Figure 4.5; Herzberg et al., 2016). Yaxley et al. (1991) showed that an infiltrating carbonatite melt would react with the surrounding peridotite wall rock consuming orthopyroxene and spinel, and crystallising clinopyroxene with secondary reactions producing minor orthopyroxene and apatite (Yaxley et al., 1991). Experiments by Wallace and Green (1988) equilibrated a carbonatite melt in a amphibole lherzolite at 21-30 kbar, which is unrealistically high for the segregation depth of Buckland basanites that are estimated to be 16-21 kbar for eastern Australia basanites (Ewart et al., 1988), resulting in the melt reacting with the spinel lherzolite wall rock similarly to how Yaxley et al. (1991) outlined. Figure 4.3 shows 100Ni/Mg plotted with 100Mn/Fe, the olivine grains also trend towards the phlogopite star from Veter et al. (2017), however the Ni/Mg number is elevated slightly offsetting it towards the pyroxenite fields from higher Ni concentrations,

driven by high modal pyroxene, and low modal olivine in the source assemblage, but mica retains the highest modal proportion (Sobolev et al., 2005, 2007; Herzberg, 2011).

Garnet is stable in pyroxene rich mantle xenoliths from eastern Australia at shallower depths than peridotite, driving a shallower garnet-spinel transition for pyroxenites in eastern Australia, estimated to be ~12 kbar (Griffin et al., 1987). So lower Yb in basanites may indicate a greater garnet signature from non-peridotite pyroxene-mica veins, than in the alkali basalts.

Apatite is also a known metasomatic mineral, and has been reported in mantle xenoliths throughout eastern Australia (O' Reilly, 1987; O'Reilly and Griffin, 2000). The formation disseminated, and veined apatite has been associated with metasomatism in the lithospheric mantle by both silica and carbonatite metasomatic agents with a hydrous component (Ionov and Hofmann, 1995). An apatite signature can been seen in the whole rock Sr enrichment and P trough (Figure 3.3), and in the elevated P_2O_5 (0.37–1.73 wt. %), which is marginally higher than P_2O_5 content found in Dubbo, which identified apatite in the source assemblage (Zhang and O'Reilly, 1997). The U depletion seen in Figure 3.3 may also a result of apatite or possibly zircon in the source assemblage, however apatite is favoured here since it has been documented in other eastern Australian intraplate provinces unlike zircon (O'Reilly and Griffin, 2000; Ionov and Hofmann, 1995; Prowatke and Klemme, 2006). Metasomatic apatite is capable of sequestering CO_2 and H_2O, which may provide a mechanism to sequester the volatiles noted by Skae (1998) in primitive Buckland basanites (O'Reilly and Griffin, 2000). But, currently there are no useful olivine minor or trace element indicators for apatite, but there are promising signs for high Ce/La ratios. High Ce/La ratios are present in both high ($Fo_{>87.5}$) and low Fo olivines ($Fo_{<87.5}$) from Buckland. But, at the time of writing there is no way of discriminating whether they are apatite indicators, or from some other process. Other potential indicators are P and Sr, however these elements are also enriched in other peridotite and non-peridotite mantle minerals, and are affected from fluid infiltration and depletion (Batanova et al., 2015).

The scale dilemma

The minerals in a non-peridotite veined component of a source assemblage have lower solidi than the peridotite wall components, so the scale of a partial melting event, along with the scale of a metasomatic event is important since the non-peridotite veined material will enter a primary melt before peridotite wall material (Foley, 1992). Small degrees of partial melting will preferentially incorporate the non-peridotite component, whereas higher degrees of partial melting will incorporate more peridotite wall material. Vice versa, if there is a large scale of mantle metasomatism percolating

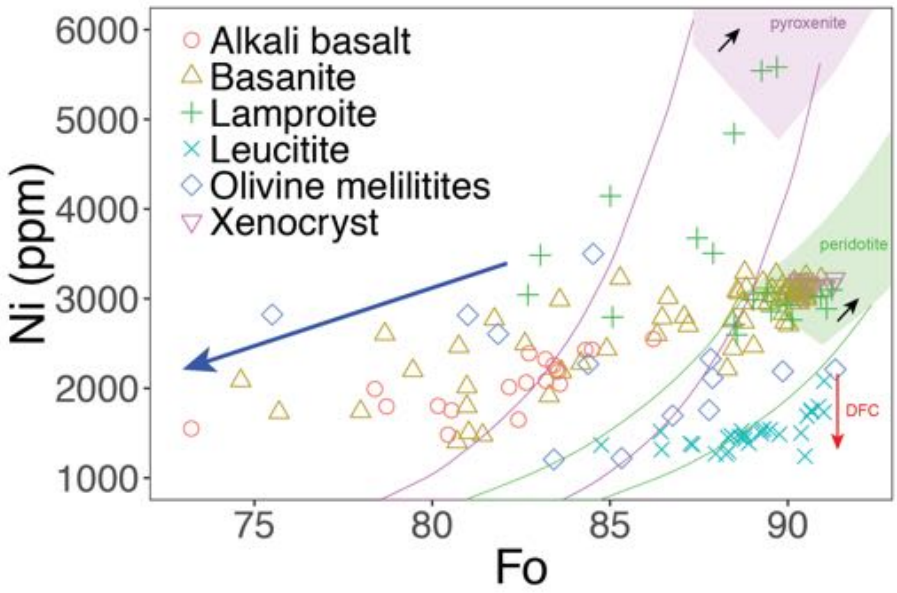

Figure 4.5: Ni plotted against Fo concentrations in olivine. Ni is from LA-ICP-MS and Fo data is from EPMA. The purple field is where olivines in a primary melt from a pyroxenite source would crystallised, while the green field represents olivine is a primary melt from a peridotite source. The small black arrows indicate where olivines would crystallised depending on the degree of depletion in the source. The purple and green lines show fractionation pathways for olivines between 0 and 20% depetion in the pyroxenite (purple), and peridotite (green). The blue line shows a mixing trend between the peridotites and pyroxenites. The source fields, fractionation pathways, and mixing lines are from Straub et al. (2008). The alkali basalts, basanites, and xenocrysts are from this study, while lamproite and leucitite data is from (Ammannati et al., 2016), and olivine melilities is from Day et al. (2014). High Fo olivines from xenocrysts and basanites plot in the peridotite field. $Fo_{>88}$ has a flat fractionation line, which follows the mixing trend from Straub et al. (2008), and likely is from the involvement of pyroxene in non-peridotite veins, and peridotite wall rock melting together.

through a peridotite there will be more veined non-peridotite material with depth. This study does not perform any geothermometry or geobarometry on the samples, however elements which are substituted into olivine favourably at higher pressures indicate that some olivines crystallised in a melt at greater depth, likely the carbonatite metasomatic agent. However, they also suggest the basanites segregated at greater depth than the alkali basalts. The Yb in basanites is also lower, which also may indicate garnet in the non-peridotite domains of the source, whereas this may have tranistioned to spinel at shallower depth in the alkali basalts. Higher Ni and higher Mn/Fe indicates the basanite source assemblage has higher proportions of pyroxene and mica in the source assemblage, likely a result of more vein material with depth.

Chapter 5

Conclusions

5.1 Source assemblage model for Buckland Volcanic Province

Whole rock and olivine chemistry data present here suggests the source assemblage Buckland Volcanic Province is a spinel lherzolite veined by varying amounts of olivine-clinopyroxene-glimmerite ± apatite. The non-peridotite component to the source assemblage was emplaced by an oxidised carbonatite metasomatic agent that formed underneath cratonic Australia. The carbonatite melt brought up phlogopite and fractionated during its accent, which produced olivine with high concentrations of pressure dependant elements and stabilised phlogopite. At ~20 kbar the carbonatite metasomatism reacted with the spinel lherzolite wall material producing veins of olivine-clinopyroxene-glimmerite ± apatite (Figure 5.1). During hot-spot induced melting the basanites were produced and segregated first, followed by the alkali basalts. The deeper basanites have a higher proportion of vein material compared to wall spinel lherzolite than the alkali basalts, resulting in the basanites retaining a more significant phlogopite/mica, and pyroxene signature than the alkali basalts. The olivine peridotite xenocrysts with sinusoidal REE patterns could have been entrained either as the carbonatite metasomatic agent rose, or as the basanite or alkai basalt melt rose to the surface.

5.2 Future directions

Analysing olivine minor and trace elements for source assemblage identification is a relatively new, and rapidly changing field, that needs further development. More experiments, like those of Förster et al. (2018) which combine peridotite and non-peridotite components are essential to better constrain partitioning behaviours of elements able to identify source components. More robust identification of peridotite xenocrysts is needed, especially since assemblages are heterogeneous between peridotite and non-peridotite components. Establishing protocols for olivine to routinely identify minor and trace isotopic signatures (Tanimizu et al., 2013), interference free trace and ultra trace element concentrations *in situ* with tandem quadrupole LA-ICP-MS/MS (Balcaen et al., 2015), and further development of protocols which allow for better comparisons between LA-ICP-MS and EMPA data.

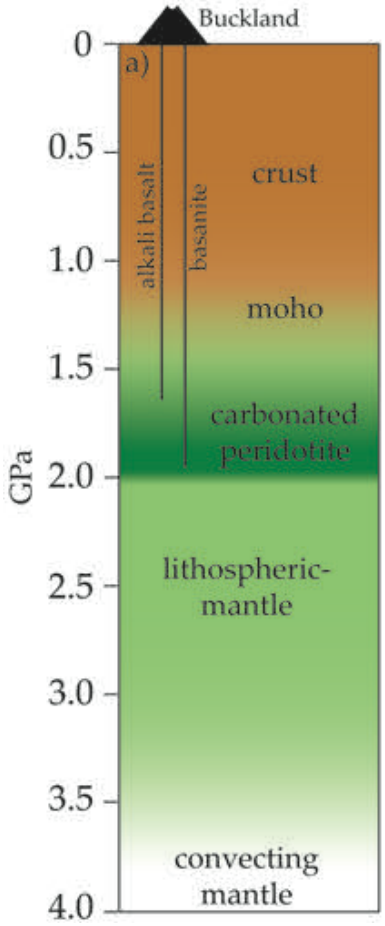

Figure 5.1: Schematic cross section of the lithosphere and upper aesthenosphere underneath Buckland Volcanic Province. Moho depth is based on Kennett et al. (2011), and LAB is based on data from Davies et al. (2015). Dark green area represents where a carbonatite metasomatic agent has reacted with spinel-peridotite forming the glimmerite veining, with the dark shading representing higher vein to wall rock ratios.

References

Ammannati, E., Jacob, D. E., Avanzinelli, R., Foley, S. F., and Conticelli, S. (2016). Low Ni olivine in silica-undersaturated ultrapotassic igneous rocks as evidence for carbonate metasomatism in the mantle. *Earth and Planetary Science Letters*, 444(Supplement C):64–74.

Balcaen, L., Bolea-Fernandez, E., Resano, M., and Vanhaecke, F. (2015). Inductively coupled plasma âĂŞ Tandem mass spectrometry (ICP-MS/MS): A powerful and universal tool for the interference-free determination of (ultra)trace elements - A tutorial review. *Analytica Chimica Acta*, 894:7–19.

Batanova, V. G., Sobolev, A. V., and Kuzmin, D. V. (2015). Trace element analysis of olivine: High precision analytical method for JEOL JXA-8230 electron probe microanalyser. *Chemical Geology*, 419:149–157.

Beattie, P., Ford, C., and Russell, D. (1991). Partition coefficients for olivine-melt and orthopyroxene-melt systems. *Contributions to Mineralogy and Petrology*, 109(2):212–224.

Berry, A. J., Hermann, J., O'Neill, H. S. C., and Foran, G. J. (2005). Fingerprinting the water site in mantle olivine. *Geology*, 33(11):869–872.

Berry, A. J., O'Neill, H. S., Hermann, J., and Scott, D. R. (2007a). The infrared signature of water associated with trivalent cations in olivine. *Earth and Planetary Science Letters*, 261(1-2):134–142.

Berry, A. J., Walker, A. M., Hermann, J., O'Neill, H. S., Foran, G. J., and Gale, J. D. (2007b). Titanium substitution mechanisms in forsterite. *Chemical Geology*, 242(1-2):176–186.

Biedermann, A. R., Pettke, T., Reusser, E., and Hirt, A. M. (2014). Anisotropy of magnetic susceptibility in natural olivine single crystals. *Geochemistry, Geophysics, Geosystems*, 15(7):3051–3065.

Birle, J. D., Gibbs, G. V., Moore, P. B., and Smith, J. V. (1968). Crystal Structure of Natural Olivines. *The American Mineralogist*, 53(May-June):807–824.

Brey, G. P. and Köhler, T. (1990). Geothermobarometry in Four-phase Lherzolites II. New Thermobarometers, and Practical Assessment of Existing Thermobarometers. *Journal of Petrology*, 31(6):1353–1378.

Burns, R. (1970). Site preferences of transition metal ions in silicate crystal structures. *Chemical Geology*, 5(4):275–283.

Bussweiler, Y., Brey, G., Pearson, D., Stachel, T., Stern, R., Hardman, M., Kjarsgaard, B., and Jackson, S. (2017). The aluminum-in-olivine thermometer for mantle peridotites - Experimental versus empirical calibration and potential applications. *Lithos*, 272-273:301–314.

Cherniak, D. J. and Liang, Y. (2014). Titanium diffusion in olivine. *Geochimica et Cosmochimica Acta*, 147:43–57.

Cohen, B. E., Knesel, K. M., Vasconcelos, P. M., and Schellart, W. P. (2013). Tracking the Australian plate motion through the Cenozoic: Constraints from 40Ar/39Ar geochronology. *Tectonics*, 32(5):1371–1383.

Cohen, B. E., Vasconcelos, P. M., and Knesel, K. M. (2007). 40Ar/39Ar constraints on the timing of Oligocene intraplate volcanism in southeast Queensland. *Australian Journal of Earth Sciences*, 54(1):105–125.

Davies, D. R. and Rawlinson, N. (2014). On the origin of recent intraplate volcanism in Australia. *Geology*, 42(12):1031–1034.

Davies, D. R., Rawlinson, N., Iaffaldano, G., and Campbell, I. H. (2015). Lithospheric controls on magma composition along Earth's longest continental hotspot track. *Nature*, 525(7570):511–514.

Day, J. M. D., Peters, B. J., and Janney, P. E. (2014). Oxygen isotope systematics of South African olivine melilitites and implications for HIMU mantle reservoirs. *Lithos*, 202-203:76–84.

De Hoog, J. C. M., Gall, L., and Cornell, D. H. (2010). Trace-element geochemistry of mantle olivine and application to mantle petrogenesis and geothermobarometry. *Chemical Geology*, 270(1):196–215.

Deer, W. A., Howie, R. A., and Zussman, J. (1997). *Rock-forming Minerals*, volume 2d ed. Geological Society, London.

Demidjuk, Z., Turner, S., Sandiford, M., George, R., Foden, J., and Etheridge, M. (2007). U-series isotope and geodynamic constraints on mantle melting processes beneath the Newer Volcanic Province in South Australia. *Earth and Planetary Science Letters*, 261(3-4):517–533.

Duncan, R. A. and McDougall, I. (1989). Volcanic time-space relationships. In Johnson, R. W., editor, *Intraplate Volcanism in Eastern Australia and New Zealand*, chapter 1, pages 43–54. Cambridge University Press, Cambridge.

Dupuy, C., Liotard, J. M., and Dostal, J. (1992). Zr/hf fractionation in intraplate basaltic rocks: Carbonate metasomatism in the mantle source. *Geochimica et Cosmochimica Acta*, 56(6):2417–2423.

Elliot, L. G. (1973). *Geology of the Springwood area, Denison Trough east central Queensland*. Honours thesis, University of Queensland.

Evans, T. M., Hugh, H. S., and Tuff, J. (2008). The influence of melt composition on the partitioning of REEs, Y, Sc, Zr and Al between forsterite and melt in the system CMAS. *Geochimica et Cosmochimica Acta*, 72(23):5708–5721.

Ewart, A. (1989). Fractionation, assimilation and source melting: a petrogenetic overview. In Johnson, R. W., editor, *Intraplate Volcanism in Eastern Australia and New Zealand*, chapter 5, pages 324–333. Cambridge University Press, Cambridge.

Ewart, A., Chappell, B. W., and Menzies, M. A. (1988). An Overview of the Geochemical and Isotopic Characteristics of the Eastern Australian Cainozoic Volcanic Provinces. *Journal of Petrology*, Special Vo(1):225–273.

Finn, C. A., Müller, R. D., and Panter, K. S. (2005). A Cenozoic diffuse alkaline magmatic province (DAMP) in the southwest Pacific without rift or plume origin. *Geochemistry, Geophysics, Geosystems*, 6(2).

Fishwick, S. and Rawlinson, N. (2012). 3-D structure of the Australian lithosphere from evolving seismic datasets. *Australian Journal of Earth Sciences*, 59(6):809–826.

Foley, S. (1992). Vein-plus-wall-rock melting mechanisms in the lithosphere and the origin of potassic alkaline magmas. *Lithos*, 28(3-6):435–453.

Foley, S. F., Jacob, D. E., and O'Neill, H. S. C. (2011). Trace element variations in olivine phenocrysts from Ugandan potassic rocks as clues to the chemical characteristics of parental magmas. *Contributions to Mineralogy and Petrology*, 162(1):1–20.

Foley, S. F. and Pintér, Z. (2018). Primary Melt Compositions in the Earth's Mantle. In *Magmas Under Pressure*, pages 3–42. Elsevier.

Foley, S. F., Prelevic, D., Rehfeldt, T., and Jacob, D. E. (2013). Minor and trace elements in olivines as probes into early igneous and mantle melting processes. *Earth and Planetary Science Letters*, 363(Supplement C):181–191.

Förster, M. W., Prelević, D., Schmück, H. R., Buhre, S., Marschall, H. R., Mertz-Kraus, R., and Jacob, D. E. (2018). Melting phlogopite-rich MARID: Lamproites and the role of alkalis in olivine-liquid Ni-partitioning. *Chemical Geology*, 476:429–440.

Frey, F. A. and Green, D. H. (1974). The mineralogy, geochemistry and origin of Iherzolite inclusions in Victorian basanites. *Geochimica et Cosmochimica Acta*, 38(7):1023–1059.

Frey, F. A., Green, D. H., and Roy, S. D. (1978). Integrated Models of Basalt Petrogenesis: A Study of Quartz Tholeiites to Olivine Melilitites from South Eastern Australia Utilizing Geochemical and Experimental Petrological Data. *Journal of Petrology*, 19(3):463–513.

Fritschle, T., Prelević, D., Foley, S. F., and Jacob, D. E. (2013). Petrological characterization of the mantle source of Mediterranean lamproites: Indications from major and trace elements of phlogopite. *Chemical Geology*, 353:267–279.

Green, D. H. and Ringwood, A. E. (1963). Mineral assemblages in a model mantle composition. *Journal of Geophysical Research*, 68(3):937–945.

Griffin, W., Sutherland, F., and Hollis, J. (1987). Geothermal profile and crust-mantle transition beneath east-central Queensland: Volcanology, xenolith petrology and seismic data. *Journal of Volcanology and Geothermal Research*, 31(3-4):177–203.

Griffin, W. L. and O'Reilly, S. Y. (1986). The lower crust in eastern Australia: xenolith evidence. *Geological Society, London, Special Publications*, 24(1):363.

Griffin, W. L., Powell, W., Pearson, N. J., and O' Reilly, S. Y. (2008). Glitter: data reduction software for Laser Ablation ICP-MS. In Sylvester, P., editor, *Laser Ablation-ICP-MS in the Earth Sciences: Current and Outstanding Issues*, pages 308–311. Mineralogical Association of Canada.

Gurnis, M., Müller, R. D., and Moresi, L. (1998). Cretaceous Vertical Motion of Australia and the AustralianAntarctic Discordance. *Science*, 279(5356):1499 LP – 1504.

Herzberg, C. (2011). Identification of Source Lithology in the Hawaiian and Canary Islands: Implications for Origins. *Journal of Petrology*, 52(1):113–146.

Herzberg, C., Asimow, P. D., Ionov, D. A., Vidito, C., Jackson, M. G., and Geist, D. (2013). Nickel and helium evidence for melt above the core-mantle boundary. *Nature*, 493:393.

Herzberg, C., Cabral, R. A., Jackson, M. G., Vidito, C., Day, J. M. D., and Hauri, E. H. (2014). Phantom Archean crust in Mangaia hotspot lavas and the meaning of heterogeneous mantle. *Earth and Planetary Science Letters*, 396(Supplement C):97–106.

Herzberg, C., Vidito, C., and Starkey, N. A. (2016). Nickel-cobalt contents of olivine record origins of mantle peridotite and related rocks. *American Mineralogist*, 101(9):1952–1966.

Horn, I., Foley, S. F., Jackson, S. E., and Jenner, G. A. (1994). Experimentally determined partitioning of high field strength- and selected transition elements between spinel and basaltic melt. *Chemical Geology*, 117(1):193–218.

Ionov, D. A. and Hofmann, A. W. (1995). Nb-Ta-rich mantle amphiboles and micas: Implications for subduction-related metasomatic trace element fractionations. *Earth and Planetary Science Letters*, 131(3):341–356.

Irvine, T. N. and Baragar, W. R. A. (1971). A Guide to the Chemical Classification of the Common Volcanic Rocks. *Canadian Journal of Earth Sciences*, 8(5):523–548.

Jaques, A. L. and Foley, S. F. (2018). Insights into the petrogenesis of the West Kimberley lamproites from trace elements in olivine. *Mineralogy and Petrology*.

Jessop, K. (2012). *Intrusions, dykes, plugs and flows of the Buckland Tertiary Basalt Province, Central Queensland*. Msc thesis, Macquarie University.

Jochum, K. P., Weis, U., Stoll, B., Kuzmin, D., Yang, Q., Raczek, I., Jacob, D. E., Stracke, A., Birbaum, K., Frick, D. A., Günther, D., and Enzweiler, J. (2011). Determination of Reference Values for NIST SRM 610-617 Glasses Following ISO Guidelines. *Geostandards and Geoanalytical Research*, 35(4):397–429.

Jochum, K. P., Willbold, M., Raczek, I., Stoll, B., and Herwig, K. (2007). Chemical Characterisation of the USGS Reference Glasses GSA-1G, GSC-1G, GSD-1G, GSE-1G, BCR-2G, BHVO-2G and BIR-1G Using EPMA, ID-TIMS, ID-ICP-MS and LA-ICP-MS. *Geostandards and Geoanalytical Research*, 29(3):285–302.

Johnson, R. W. and Wellman, P. (1989). Framework for Volcanism. In Johnson, R. W., editor, *Intraplate Volcanism in Eastern Australia and New Zealand*, chapter 1, pages 1–53. Cambridge University Press, Cambridge.

Jones, I. and Verdel, C. (2015). Basalt distribution and volume estimates of Cenozoic volcanism in the Bowen Basin region of eastern Australia: Implications for a waning mantle plume. *Australian Journal of Earth Sciences*, 62(2):255–263.

Kelemen, P. B., Hart, S. R., and Bernstein, S. (1998). Silica enrichment in the continental upper mantle via melt/rock reaction. *Earth and Planetary Science Letters*, 164(1-2):387–406.

Kennett, B. L. N., Salmon, M., Saygin, E., and Group, A. W. (2011). AusMoho: the variation of Moho depth in Australia. *Geophysical Journal International*, 187(2):946–958.

Kushiro, I., Syono, Y., and Akimoto, S. (1967). Stability of phlogopite at high pressures and possible presence of phlogopite in the earth's upper mantle. *Earth and Planetary Science Letters*, 3:197–203.

Laubier, M., Grove, T., and Langmuir, C. H. (2014). Trace element mineral/melt partitioning for basaltic and basaltic andesitic melts: An experimental and laser ICP-MS study with application to the oxidation state of mantle source regions. *Earth and Planetary Science Letters*, 392:265–278.

Le Maitre, R. W., Streckeisen, A., Zanettin, B., Le Bas, M., Bonin, B., and Bateman, P. (2004). *Igneous Rocks: A Classification and Glossary of Terms*, volume -1.

Le Roux, V., Dasgupta, R., and Lee, C.-T. (2011). Mineralogical heterogeneities in the Earth's mantle: Constraints from Mn, Co, Ni and Zn partitioning during partial melting. *Earth and Planetary Science Letters*, 307(3):395–408.

Mallmann, G., O'Neill, H. S. C., and Klemme, S. (2009). Heterogeneous distribution of phosphorus in olivine from otherwise well-equilibrated spinel peridotite xenoliths and its implications for the mantle geochemistry of lithium. *Contributions to Mineralogy and Petrology*, 158(4):485–504.

Matzen, A. K., Baker, M. B., Beckett, J. R., and Stolper, E. M. (2013). The Temperature and Pressure Dependence of Nickel Partitioning between Olivine and Silicate Melt. *Journal of Petrology*, 54(12):2521–2545.

Matzen, A. K., Baker, M. B., Beckett, J. R., Wood, B. J., and Stolper, E. M. (2017). The effect of liquid composition on the partitioning of Ni between olivine and silicate melt. *Contributions to Mineralogy and Petrology. Beitrage Zur Mineralogie Und Petrologie*, 172(1):3.

McDonough, W. F. and Sun, S.-s. (1995). The composition of the Earth. *Chemical Geology*, 120(3):223–253.

McDougall, I. and Duncan, R. A. (1980). Linear volcanic chains - recording plate motions? *Tectonophysics*, 63(1-4):275–295.

Meeuws, F. J. E., Holford, S. P., Foden, J. D., and Schofield, N. (2016). Distribution, chronology and causes of Cretaceous - Cenozoic magmatism along the magma-poor rifted southern Australian margin: Links between mantle melting and basin formation. *Marine and Petroleum Geology*, 73:271–298.

Navon, O. and Stolper, E. (1987). Geochemical Consequences of Melt Percolation: The Upper Mantle as a Chromatographic Column. *The Journal of Geology*, 95(3):285–307.

Neumann, E. R., Wulff-Pedersen, E., Pearson, N. J., and Spencer, E. A. (2002). Mantle Xenoliths from Tenerife (Canary Islands): Evidence for Reactions between Mantle Peridotites and Silicic Carbonatite Melts inducing Ca Metasomatism. *Journal of Petrology*, 43(5):825–857.

Neumann, E.-R., Wulff-Pedersen, E., Simonsen, S. L., Pearson, N. J., Martí, J., and Mitjavila, J. (1999). Evidence for Fractional Crystallization of Periodically Refilled Magma Chambers in Tenerife, Canary Islands. *Journal of Petrology*, 40(7):1089–1123.

Nielsen, R. L., Gallahan, W. E., and Newberger, F. (1992). Experimentally determined mineral-melt partition coefficients for Sc, Y and REE for olivine, orthopyroxene, pigeonite, magnetite and ilmenite. *Contributions to Mineralogy and Petrology*, 110(4):488–499.

O' Reilly, S. Y. (1987). Volatile-rich mantle beneath eastern Australia. In *Mantle Xenoliths*, chapter 45, pages 661 – 672. Wiley.

Onuma, K. and Tohara, T. (1983). Effect of chromium on phase relations in the join forsterite-anorthite-diopside in air at 1 Atm. *Contributions to Mineralogy and Petrology*, 84(2):174–181.

O'Reilly, S. Y., Chen, D., Griffin, W. L., and Ryan, C. G. (1997). Minor elements in olivine from spinel lherzolite xenoliths: implications for thermobarometry. *Mineralogical Magazine*, 61(405):257–269.

O'Reilly, S. Y. and Griffin, W. L. (1987). *Eastern Australia - 4000 kilometres of mantle samples*. Wiley, Chichester, UK.

O'Reilly, S. Y. and Griffin, W. L. (2000). Apatite in the mantle: implications for metasomatic processes and high heat production in Phanerozoic mantle. *Lithos*, 53(3):217–232.

O'Reilly, S. Y. and Griffin, W. L. (2013). Mantle Metasomatism. In Harlov, D. E. and Austrheim, H., editors, *Metasomatism and the Chemical Transformation of Rock: The Role of Fluids in Terrestrial and Extraterrestrial Processes*, pages 471–533. Springer Berlin Heidelberg, Berlin, Heidelberg.

O'Reilly, S. Y., Griffin, W. L., and Stabel, A. (1988). Evolution of Phanerozoic Eastern Australian Lithosphere: Isotopic Evidence for Magmatic and Tectonic Underplating. *Journal of Petrology*, Special_Vo(1):89–108.

O'Reilly, S. Y. and Zhang, M. (1995). Geochemical characteristics of lava-field basalts from eastern Australia and inferred sources: Connections with the subcontinental lithospheric mantle? *Contributions to Mineralogy and Petrology*, 121(2):148.

Palme, H. and O'Neill, H. (2014). Cosmochemical Estimates of Mantle Composition. In *Treatise on Geochemistry: Second Edition*, volume 3, pages 1–39. Elsevier.

Papike, J. J., Karner, J. M., and Shearer, C. K. (2005). Comparative planetary mineralogy: Valence state partitioning of Cr, Fe, Ti, and V among crystallographic sites in olivine, pyroxene, and spinel from planetary basalts.

Prelević, D., Jacob, D. E., and Foley, S. F. (2013). Recycling plus: A new recipe for the formation of Alpine-Himalayan orogenic mantle lithosphere. *Earth and Planetary Science Letters*, 362(Supplement C):187–197.

Prowatke, S. and Klemme, S. (2006). *Trace element partitioning between apatite and silicate melts*, volume 70.

Roeder, P. L. and Emslie, R. F. (1970). Olivine-liquid equilibrium. *Contributions to Mineralogy and Petrology*, 29(4):275–289.

Rosenthal, A., Foley, S., Pearson, D., Nowell, G., and Tappe, S. (2009). Petrogenesis of strongly alkaline primitive volcanic rocks at the propagating tip of the western branch of the East African Rift. *Earth and Planetary Science Letters*, 284(1-2):236–248.

Rudnick, R. (1994). *Northern Tanzanian peridotite xenoliths: a comparison with Kaapvaal peridotites and inferences on metasomatic interactions*.

Seitz, H.-M. and Woodland, A. B. (2000). The distribution of lithium in peridotitic and pyroxenitic mantle lithologies - an indicator of magmatic and metasomatic processes. *Chemical Geology*, 166(1):47–64.

Shannon, R. (1976). Revised effective ionic radii and systematic studies of interatomic distances in halides and chalcogenides. *Acta Crystallographica Section A*, 32(5):751–767.

Skae, A. (1998). *The petrology of the Buckland volcanic province, Central Queensland, Australia*. Phd, University of Oxford.

Sobolev, A. V., Hofmann, A. W., Kuzmin, D. V., Yaxley, G. M., Arndt, N. T., Chung, S.-L., Danyushevsky, L. V., Elliott, T., Frey, F. A., Garcia, M. O., Gurenko, A. A., Kamenetsky, V. S., Kerr, A. C., Krivolutskaya, N. A., Matvienkov, V. V., Nikogosian, I. K., Rocholl, A., Sigurdsson, I. A., Sushchevskaya, N. M., and Teklay, M. (2007). The Amount of Recycled Crust in Sources of Mantle-Derived Melts. *Science*, 316(5823):412.

Sobolev, A. V., Hofmann, A. W., Sobolev, S. V., and Nikogosian, I. K. (2005). An olivine-free mantle source of Hawaiian shield basalts. *Nature*, 434(7033):590–597.

Sobolev, N. V., Logvinova, A. M., Zedgenizov, D. A., Pokhilenko, N. P., Malygina, E. V., Kuzmin, D. V., and Sobolev, A. V. (2009). Petrogenetic significance of minor elements in olivines from diamonds and peridotite xenoliths from kimberlites of Yakutia. *Lithos*, 112:701–713.

Stead, C. V., Tomlinson, E. L., Kamber, B. S., Babechuk, M. G., and McKenna, C. A. (2017). Rare Earth Element Determination in Olivine by Laser Ablation-Quadrupole-ICP-MS: An Analytical Strategy and Applications. *Geostandards and Geoanalytical Research*, 41(2):197–212.

Straub, S. M., LaGatta, A. B., Martin-Del Pozzo, A. L., and Langmuir, C. H. (2008). Evidence from high-Ni olivines for a hybridized peridotite/pyroxenite source for orogenic andesites from the central Mexican Volcanic Belt. *Geochemistry, Geophysics, Geosystems*, 9(3):n/a–n/a.

Sun, S. and McDonough, W. F. (1989). Chemical and isotopic systematics of oceanic basalts: implications for mantle composition and processes. *Geological Society, London, Special Publications*, 42(1):313 – 345.

Sutherland, F. (1981). Migration in relation to possible tectonic and regional controls in eastern Australian volcanism. *Journal of Volcanology and Geothermal Research*, 9(2-3):181–213.

Sutherland, F. L., Graham, I. T., Meffre, S., Zwingmann, H., and Pogson, R. E. (2012). Passive-margin prolonged volcanism, East Australian Plate: outbursts, progressions, plate controls and suggested causes. *Australian Journal of Earth Sciences*, 59(7):983–1005.

Tanimizu, M., Sugiyama, N., Ponzevera, E., and Bayon, G. (2013). Determination of ultra-low 236U/238U isotope ratios by tandem quadrupole ICP-MS/MS. *Journal of Analytical Atomic Spectrometry*, 28(9):1372–1376.

Tappe, S., Foley, S. F., Jenner, G. A., Heaman, L. M., Kjarsgaard, B. A., Romer, R. L., Stracke, A., Joyce, N., and Hoefs, J. (2006). Genesis of Ultramafic Lamprophyres and Carbonatites at Aillik Bay, Labrador: a Consequence of Incipient Lithospheric Thinning beneath the North Atlantic Craton. *Journal of Petrology*, 47(7):1261–1315.

Taura, H., Yurimoto, H., Kurita, K., and Sueno, S. (1998). Pressure dependence on partition coefficients for trace elements between olivine and the coexisting melts. *Physics and Chemistry of Minerals*, 25(7):469–484.

Vasconcelos, P. M., Knesel, K. M., Cohen, B. E., and Heim, J. A. (2008). Geochronology of the Australian Cenozoic: a history of tectonic and igneous activity, weathering, erosion, and sedimentation. *Australian Journal of Earth Sciences*, 55(6-7):865–914.

Veter, M., Foley, S. F., Mertz-Kraus, R., and Groschopf, N. (2017). Trace elements in olivine of ultramafic lamprophyres controlled by phlogopite-rich mineral assemblages in the mantle source. *Lithos*, 292-293(Supplement C):81–95.

Wallace, M. E. and Green, D. H. (1988). An experimental determination of primary carbonatite magma composition. *Nature*, 335:343.

Waltenburg, K. (2006). *Geochronology of weathered basaltic flows at Carnavon Gorge*. Honours thesis, University of Queensland.

Wellman, P. and McDougall, I. (1974). Cainozoic igneous activity in eastern australia. *Tectonophysics*, 23(1):49–65.

Whitehead, P. W., Stephenson, P. J., McDougall, I., Hopkins, M. S., Graham, A. W., Collerson, K. D., and Johnson, D. P. (2007). Temporal development of the Atherton Basalt Province, north Queensland. *Australian Journal of Earth Sciences*, 54(5):691–709.

Wood, B. and Blundy, J. (2003). Trace Element Partitioning under Crustal and Uppermost Mantle Conditions: The Influences of Ionic Radius, Cation Charge, Pressure, and Temperature. *Treatise on Geochemistry*, pages 395–424.

Wyllie, P. J., Huang, W.-L., Otto, J., and Byrnes, A. P. (1983). Carbonation of peridotites and decarbonation of siliceous dolomites represented in the system CaO-MgO-SiO2-CO2 to 30 kbar. *Tectonophysics*, 100(1):359–388.

Yaxley, G. M., Crawford, A. J., and Green, D. H. (1991). Evidence for carbonatite metasomatism in spinel peridotite xenoliths from western Victoria, Australia. *Earth and Planetary Science Letters*, 107(2):305–317.

Yaxley, G. M. and Green, D. H. (1998). Reactions between eclogite and peridotite: mantle refertilisation by subduction of oceanic crust. *Schweiz. Mineral. Petrogr. Mitt*, 78(2):243–255.

Yaxley, G. M., Green, D. H., and Kamenetsky, V. (1998). Carbonatite Metasomatism in the Southeastern Australian Lithosphere. *Journal of Petrology*, 39(11-12):1917–1930.

Zanetti, A., Tiepolo, M., Oberti, R., and Vannucci, R. (2004). Trace-element partitioning in olivine: modelling of a complete data set from a synthetic hydrous basanite melt. *Lithos*, 75(1-2):39–54.

Zhang, M. and O'Reilly, S. Y. (1997). Multiple sources for basaltic rocks from Dubbo, eastern Australia: geochemical evidence for plume-lithospheric mantle interaction. *Chemical Geology*, 136(1):33–54.

Appendix

On the following pages the standards used for LA-ICP-MS, XRF, and Solution ICP-MS analysis are compared with GeoRem preferred values (http://georem.mpch-mainz.gwdg.de/start.asp?dataversion=current).

Table 1: LA-ICP-MS data for NIST612 and BCR-2G compared to GeoRem preferred values. Used for acquiring olivine trace element concentrations.

Sample	LA-ICP-MS							
Lithology	NIST612		GeoRem		BCR-2G		GeoRem	
	n=29	1σ		1σ	n=29	1σ		1σ
Li (ppm)	40.5	1.4	40.2	1.3	9.0	0.2	9	1
Al_2O_3	2.03	0.04	2.03	0.04	13.4	0.3	13.4	0.4
P*	46.6	2.5	46.6	6.9	0.37	0.01	0.37	0.01
V	39.0	0.9	38.8	1.2	426	8	425	18
Cr	36.5	0.5	36.4	1.5	17	0.4	17	2
Mn	38.8	0.6	38.7	0.9	1551	19.2	1550	70
Co	35.6	0.4	35.5	1	38	0.5	38	2
Cu	37.8	0.8	37.8	1.5	21	0.6	21	5
Zn	39.5	1.8	39.1	1.7	125	3.1	125	5
Ga	36.9	0.4	36.9	1.5	23	1.7	23	0.1
Sr	78.7	1.7	78.4	0.2	342	7.6	342	4
Y	38.4	0.9	38.8	1.4	35.0	1.2	35	3
Zr	38.3	3.7	37.9	1.2	184	5.8	184	15
Nb	39.1	0.8	38.9	2.1	12.5	0.3	12.5	1
Ba	39.5	1.1	39.3	0.9	684	15.7	683	7
La	36.2	0.9	36	0.7	24.7	0.7	24.7	0.3
Ce	38.6	0.9	38.4	0.7	53.4	1.2	53.3	0.5
Gd	37.5	0.9	37.3	0.9	6.72	0.2	6.71	0.07
Yb	39.3	0.9	39.2	0.9	3.4	0.1	3.39	0.03

Table 2: XRF, and solution ICP-MA data for BHVO-2 compared to GeoRem preferred values. Used for acquiring whole rock chemistry concentrations.

Sample	XRF				Soltuion ICP-MS			
Lithology	BHVO-2		GeoRem		BHVO-2		GeoRem	
	n=10	±2σ		1σ	n=3	1σ		1σ
SiO_2 (wt.%)	49.9	0.13	49.3	0.1				
TiO_2	2.75	0.01	2.79	0.02				
Al_2O_3	13.71	0.08	13.6	0.1				
FeO_{tot}	12.48	0.01	11.3	0.1				
MnO	0.18	0.001	0.17	0.03				
MgO	7.34	0.03	3.599	0.02				
CaO	11.53	0.01	7.13	0.075				
Na_2O	2.27	0.02	2.4	0.1				
K_2O	0.51	0.01	0.51	0.02				
P_2O_5	0.28	0.01	0.29	0.02				
Li (ppm)					4.5	0.05	4.4	0.8
Be					1.5	0.01	1.3	0.2
Sc					35.2	0.5	33	2
Ti					17722	296	16300	900
V					327	6.24	308	19
Cr					240	3.56	293	12
Mn*					0.17	0.002	0.17	0.03
Co					45.4	1	44	2
Ni					133.5	4	116	7
Cu					157.4	2	127	11
Zn					105.9	1	102	6
Ga					21	0.4	22	3
Rb					9.3	0.14	9.2	0.04
Sr					381	2	396	1
Y					27	0.26	26	2
Zr					175	2	170	7
Nb					18.4	0.2	18.3	0.8
Mo					3.6	0.1	3.8	0.2
Cd					0.1	0.001	0.1	0.01
Cs					0.1	0.001	0.1	0.02
Ba					126	3	131	2
La					14.8	0.28	15.2	0.2
Ce					35.4	0.61	37.6	0.2
Pr					5.0	0.04	5.35	0.22
Nd					22.9	0.07	24.5	0.2
Sm					5.8	0.01	6.1	0.03
Eu					1.9	0.01	2.07	0.01
Tb					0.9	0.01	0.92	0.04
Gd					5.9	0.02	6.16	0.05
Dy					4.9	0.04	5.28	0.05
Ho					0.9	0.01	0.98	0.04
Er					2.4	0.04	2.56	0.02
Yb					1.8	0.01	2.01	0.02
Lu					0.3	0.001	0.279	0.003
Hf					3.9	0.04	4.32	0.18
Ta					1.0	0.01	1.15	0.1
Th					1.1	0.02	1.22	0.05
U					0.4	0.01	0.403	0.003